View metadata, citation and similar papers at core.ac.uk

brought to you by CORE

provided by NASA Technical Reports Server

NASA Technical Memorandum 102196

Study of the Integration of Wind Tunnel and Computational Methods for Aerodynamic Configurations

Lindsey E. Browne and Dale L. Ashby

October 1989

(NASA-TM-102196) STUDY OF THE INTEGRATION
OF WIND TUNNEL AND COMPUTATIONAL METHODS FOR
AERODYNAMIC CONFIGURATIONS (NASA) 69 p
CSCL 01A

N90-13332

Unclas
G3/02 0251710

National Aeronautics and
Space Administration

NASA Technical Memorandum 102196

Study of the Integration of Wind Tunnel and Computational Methods for Aerodynamic Configurations

Lindsey E. Browne and Dale L. Ashby, Ames Research Center, Moffett Field, California

October 1989

NASA
National Aeronautics and
Space Administration

Ames Research Center
Moffett Field, California 94035

TABLE OF CONTENTS

Page

LIST OF SYMBOLS v

SUMMARY 1

1. INTRODUCTION 1

2. THEORY 3

  2.1 The Mathematical Model 3

    2.1.1 Shortcomings of Potential Flow-Based Computer Codes 9

    2.1.2 Method of Removing the Wind Tunnel Walls 10

    2.1.3 Calculation of the Wall Correction Factor 10

3. DISCUSSION OF RESULTS 11

  3.1 Case One: The Two-Dimensional, High-Lift Wing 11

    3.1.1 Verification of the Computer Model 11

    3.1.2 Wall Correction Computed by PMARC 12

    3.1.3 Wall Correction Comparison 13

  3.2 Case Two: The F/A-18 Aircraft Model 13

    3.2.1 Model Fabrication and Wind Tunnel Apparatus 13

    3.2.2 Validation of the Wind Tunnel Test 13

    3.2.3 Verification of the Computer Model 14

    3.2.4 Wall Corrections Computed by PMARC 15

4. CONCLUSIONS 17

PRECEDING PAGE BLANK NOT FILMED

PAGE ii INTENTIONALLY BLANK

APPENDIX A. SOLUTION OF THE DOUBLET CONTRIBUTION TO THE INDUCED VELOCITY 19

APPENDIX B. SOLUTION OF THE SOURCE CONTRIBUTION TO THE INDUCED VELOCITY 23

APPENDIX C. PANEL ANALYSIS 31

REFERENCES 43

LIST OF SYMBOLS

$\vec{a}$	Vector from a panel corner point to a velocity scan point
A	Magnitude of vector $\vec{a}$
Area	Area of a panel
$\vec{b}$	Vector from a panel corner point on the same side as vector $\vec{a}$ to a velocity scan point
B	Magnitude of vector $\vec{b}$
B_{JK}	Velocity potential influence coefficient at point J due to a uniform source distribution over panel K
C_D	Coefficient of drag
C_{JK}	Velocity potential influence coefficient at point J due to a uniform doublet distribution over panel K
C_L	Lift coefficient
C_M	Pitching moment coefficient
C_P	Pressure coefficient
dS	Differential surface area element
$\vec{l}, \vec{m}, \vec{n}$	Panel unit vectors in local coordinate system
N_S	Total number of surface panels
P	An arbitrary point in space
q_c	Corrected dynamic pressure
q_m	Measured dynamic pressure
$\vec{r}$	Vector between a point P and an element dS
S	Configuration surface
S_∞	Imaginary surface at infinity
$\vec{V}$	Velocity vector

V	Velocity vector magnitude
$\vec{V}_{\mu_{PK}}$	Velocity influence coefficient at point P due to a uniform doublet distribution on panel K
$\vec{V}_{\sigma_{PK}}$	Velocity influence coefficient at point P due to a uniform source distribution on panel K
W	Wake surface
Φ	Total velocity potential
ϕ	Perturbation velocity potential
ϕ_∞	Free-stream velocity potential
μ	Doublet singularity strength per unit area
σ	Source singularity strength per unit area

Subscripts:

i	Interior region
J	Refers to panel J
K	Refers to panel K
L	Lower surface of a panel
P	Refers to a velocity scan point P
U	Upper surface of a panel
w	Refers to the presence of the wind tunnel walls in a PMARC model
nw	Refers to the absence of the wind tunnel walls in a PMARC model

SUMMARY

A study was conducted to determine the effectiveness of using a low-order panel code to estimate wind tunnel wall corrections. The corrections were found by two computations. The first computation included the test model and the surrounding wind tunnel walls, while in the second computation the wind tunnel walls were removed. The difference between the force and moment coefficients obtained by comparing these two cases allowed the determination of the wall corrections. The technique was verified by matching the test-section, wall-pressure signature from a wind tunnel test with the signature predicted by the panel code (Panel Method Ames Research Center (PMARC)). To prove the viability of the technique, two cases were considered. The first was a two-dimensional high-lift wing with flap that was tested in the 7- by 10-Foot Wind Tunnel at NASA Ames Research Center. The second was a 1/32-scale model of the F/A-18 aircraft which was tested in the low-speed wind tunnel at San Diego State University. Results of this study indicate that the proposed wind tunnel wall correction method is comparable to other methods and that it also inherently includes the corrections resulting from model blockage and wing lift.

1. INTRODUCTION

Wind tunnels provide a well-controlled environment which is free of atmospheric hazards for aerodynamic measurements. One of the typical problems associated with a wind tunnel test is the error introduced into the measurements by the presence of the wind tunnel walls. Since the flow in a wind tunnel is constrained by the walls, it must accelerate around the model in order to satisfy the continuity equation. As a result, the model behaves inside the wind tunnel as if it were at a slightly greater speed than the nominal wind tunnel velocity (ref. 1).

The increased velocity or dynamic pressure, caused by the solid blockage of the model, results in an increase in all the forces and moments acting on the model. Because the velocity in the viscous wake is slower than the velocity in the free stream, an additional blockage, known as wake blockage, is created. As the wake grows, the free-stream velocity must increase, again as defined by the continuity equation. The increase in velocity around the model and its wakes causes a pressure gradient to develop (according to the Bernoulli equation) which creates an apparent increase in drag on the model. A blockage correction is needed to be able to determine the incremental velocity that, when added to the free stream, accounts for the extra forces and moments. Once the velocity increment is found, the aerodynamic data can be "corrected" to obtain the desired free-air results.

The angle of attack of the model is also affected by the wind tunnel boundaries. The presence of the wind tunnel walls alters the normal curvature of the flow around the test body, creating an apparent increase in the angle of attack (ref. 1). To complete the wind tunnel wall corrections, the geometric angle of attack needs to be corrected for this apparent increase. In this study, however, only the dynamic pressure correction was calculated, although the angle-of-attack correction can be determined using the same numerical technique.

Most methods for determining the dynamic pressure correction take a mathematical approach based on aerodynamic potential theory. Using a potential flow model, a solid body can be simulated with a source-sink system while the wake is simulated with doublets. Early methods, such as Herriot's (ref. 2), attempt to represent the solid blockage by using images. Herriot simulates the model with a source-sink distribution and the walls with an infinite distribution of source-sink images. The correction is found by summing up the effect of the images alone. Maskell (ref. 3) uses a similar methodology to determine the increase in drag. In this method, the wake blockage is replaced by a source which, because of continuity, is matched by a downstream sink of the same strength. Images in this model are composed of a doubly infinite source-sink system which is spaced one tunnel height apart vertically and one tunnel width apart horizontally (ref. 4). The incremental increase in velocity due to the images is the source strength divided by twice the width of the jet multiplied by the height of the tunnel. The increased drag can then be easily found from the incremental velocity.

Another approach to the problem is the wall-pressure signature method developed by Hackett (ref. 5). Hackett uses an inverse method to determine the strengths of a series of sources and sinks that, when acted upon by an appropriate wall-image system, will produce the same pressure signature observed during the test. In this method, the solid and wake blockages are handled separately. The wake blockage is found by matching the actual wake pressure signature with a signature generated by a potential source image system. The correction is derived by finding the influence of the image system alone. The surface blockage is handled in the same manner.

Similarly, it is possible to determine the correction by using panel methods. Low-order panel codes model the geometry of a body with a series of panels. A flow field is generated by distributing source and/or doublet singularities over the panels. Once a problem is modeled correctly, the panel codes can determine the forces, moments, and pressures acting on the body. To determine the wall corrections by this method, two computations are necessary. The first computation models the geometry of the test body and the wind tunnel walls, while the second computation models only the geometry of the test body. The validity of the first computation is evaluated by comparing the wall-pressure signature obtained in the wind tunnel test at the centerline of the test section with the signature calculated by the panel code. If the signatures match, then the tunnel walls are mathematically removed from the computer model and the forces, moments, and pressures are recalculated. The difference between the two cases is the correction.

Two cases were studied to demonstrate the method. The first case was a two-dimensional, high-lift wing with a single flap which was tested in the 7- by 10-Foot Wind Tunnel at NASA Ames Research Center (ARC) (ref. 6). The second case was a 1/32-scale model of an F/A-18 aircraft which was tested in the low-speed wind tunnel at San Diego State University (SDSU). A low-order panel code, Panel Method Ames Research Center (PMARC) (ref. 7), which is being developed at ARC, was used for the computations. The cases were chosen to show the versatility of the code to handle a relatively simple geometry, the two-dimensional wing and flap, and a complex geometry consisting of a three-dimensional fighter. After a review of the mathematical model in chapter 2, the results from the test cases are presented in chapter 3.

2. THEORY

2.1 The Mathematical Model

In this chapter a brief description of the important principles of panel methods will be provided. These methods, as well as the current low-order panel code (PMARC) are based on potential-flow theory. The steady-state flow is considered to be irrotational, incompressible, and inviscid, and must therefore satisfy Laplace's equation

$$\nabla^2\Phi = 0 \tag{1}$$

applied over a control volume. The closed surface of a body divides the flow field into two regions—an inner region and an outer region—as shown in figure 1, where both flows satisfy equation (1). For most applications, the flow field outside the body is the region of interest. The boundary conditions for equation (1) are

1. The normal velocities across the body's solid boundaries must be equal to zero or a prescribed value.

2. The flow disturbance due to the model must diminish far from the aircraft.

3. The flow field must satisfy the Kutta condition along sharp trailing edges to fix the circulation.

Equation (1) is solved by applying Green's Identity to the volume encompassed by both flow regions. The resulting surface integral defines the potential at any point in the region such that (ref. 8)

$$\Phi_P = \frac{1}{4\pi}\iint\limits_{S+W+S_\infty} (\Phi - \Phi_i)\vec{n}\cdot\nabla\left(\frac{1}{r}\right)dS - \frac{1}{4\pi}\iint\limits_{S+W+S_\infty} \frac{1}{r}\,\vec{n}\cdot(\nabla\Phi - \nabla\Phi_i)dS \tag{2}$$

In the integral, r is the distance from a point in a region, P, to an area element, dS, on the surface of a body or a wake. The variable $\vec{n}$ is the unit normal vector of the surface or wake element pointing into the flow and the subscript i represents the internal flow region. The first integral of equation (2) is the contribution from a distribution of doublets on the surface and wake per unit area. The second integral is the contribution from a similar distribution of sources per unit area. This equation is reduced by applying the second boundary condition and by assuming that the upper and lower wake surfaces are infinitesimally close to each other. This thin-wake assumption allows the entrainment in the wake to be neglected; therefore, the jump in the normal velocity is zero, which causes the source term to disappear from the integral (ref. 9). The simplified equation becomes

$$\Phi_P = \frac{1}{4\pi}\iint\limits_S (\Phi-\Phi_i)\vec{n}\cdot\nabla\left(\frac{1}{r}\right)dS - \frac{1}{4\pi}\iint\limits_S \frac{1}{r}\vec{n}\cdot(\nabla\Phi-\nabla\Phi_i)dS + \frac{1}{4\pi}\iint\limits_W (\Phi_U-\Phi_L)\vec{n}\cdot\nabla\left(\frac{1}{r}\right)dS + \phi_\infty \tag{3}$$

where ϕ_∞ is the free-stream potential of the boundary surface at infinity.

If point P lies on the body surface, the integrals become singular. The singularity is avoided by assuming a hemispherical deformation of the body's surface centered at P (ref. 8). In the limit where the radius of the deformation goes to zero, the resulting total potential at point P is

$$\begin{aligned}\Phi_P = {} & \frac{1}{4\pi}\iint\limits_{S-P} (\Phi-\Phi_i)\vec{n}\cdot\nabla\left(\frac{1}{r}\right)dS - \frac{1}{2}(\Phi-\Phi_i)_P - \frac{1}{4\pi}\iint\limits_S \frac{1}{r}\vec{n}\cdot(\nabla\Phi-\nabla\Phi_i)dS \\ & + \frac{1}{4\pi}\iint\limits_W (\Phi_U-\Phi_L)\vec{n}\cdot\nabla\left(\frac{1}{r}\right)dS + \phi_\infty\end{aligned} \tag{4}$$

where $1/2(\Phi-\Phi_i)_p$ is the contribution from the hemispherical deformation only. The subscript S-P denotes that the point P is excluded from the integral. Equation (4) is solved by applying the internal Dirichlet boundary condition, which assumes that the internal potential equals the onset potential. As a result, the surface singularities have to provide only the perturbation potential instead of the total potential (ref. 8). Looking at P inside the surface, equation (4) reduces to

$$\frac{1}{4\pi}\iint\limits_{S-P} \Phi\vec{n}\cdot\nabla\left(\frac{1}{r}\right)dS - \frac{1}{2}\Phi_P - \frac{1}{4\pi}\iint\limits_S \frac{1}{r}\vec{n}\cdot(\nabla\Phi-\nabla\phi_\infty)dS + \frac{1}{4\pi}\iint\limits_W (\Phi_U-\Phi_L)\vec{n}\cdot\nabla\left(\frac{1}{r}\right)dS = 0 \tag{5}$$

The doublet density on the surface exterior is defined as the perturbation potential (ref. 9)

$$4\pi\mu = \Phi - \phi_\infty = \phi \tag{6}$$

and the source density is defined as (ref. 9)

$$4\pi\sigma = -\vec{n}\cdot(\nabla\Phi - \nabla\phi_\infty) \tag{7}$$

The source strength of each singularity is found by applying the first boundary condition to equation (7). The doublet strengths are found by reducing equation (5) into a single integral which contains only the unknown singularities. This is accomplished by substituting equation (6) into equation (5). After solving for the doublet and source strengths, the potential at any point P is found by substituting σ and μ into equation (5) and solving for Φ_p, which results in

$$\Phi_P = \iint\limits_S \mu \vec{n} \cdot \nabla\left(\frac{1}{r}\right) dS + K_{\mu P} + \iint\limits_S \frac{\sigma}{r} dS + \iint\limits_W \mu \vec{n} \cdot \nabla\left(\frac{1}{r}\right) dS + \phi_\infty \tag{8}$$

In the equation, K = 0 if the point P is not on the body's surface, K = 2π if P is on a smooth part of the outer surface of the body, K = −2π if P is on a smooth part of the inner surface of the body, or if P is at a crease in the surface, then K = the solid angle contained at that crease (ref. 8).

The external velocity field is found by

$$V_P = \nabla \Phi_P \tag{9}$$

At any point P, the velocity is

$$V_P = -\iint\limits_S \mu \nabla_P\left[\vec{n} \cdot \nabla_K\left(\frac{1}{r}\right)\right] dS - \iint\limits_S \sigma \nabla_K\left(\frac{1}{r}\right) dS - \iint\limits_W \mu \nabla_P\left[\vec{n} \cdot \nabla_K\left(\frac{1}{r}\right)\right] dW + V_\infty \tag{10}$$

where ∇_P is taken with respect to the coordinates of point P and ∇_K is taken with respect to the centroid of panel K.

By breaking up the surface of a body and its wake into panels, the integrals of equations (8) and (10) can be rewritten in a discrete form. This is done by assuming that constant-strength doublets and sources are distributed on the panels and that the potential and induced velocity at a point is the sum of the influences from each panel. The unknown doublet strengths can then be found by using a set of simultaneous equations that are defined as the sum of the surface integrals of each panel. Because the source strengths are known, they are moved to the right-hand side (RHS) of the resulting matrix equation. The discrete forms of equations (8) and (10) are (ref. 9)

$$\sum_{K=1}^{N_s} (\mu_K C_{JK}) + \sum_{L=1}^{N_W} (\mu_{W_L} C_{JL}) + \sum_{K=1}^{N_S} \sigma_K B_{JK} = 0; \quad J = 1, N_S \tag{11}$$

$$\vec{V}_P = \vec{V}_\infty - \sum_{K=1}^{N_s} (\mu_k \vec{V}_{\mu PK}) - \sum_{L=1}^{N_W} (\mu_L \vec{V}_{\mu LK}) - \sum_{K=1}^{N_S} (\sigma_k \vec{V}_{\mu PK}) \tag{12}$$

where the potential influence coefficients are found by evaluating the gradients from equation (10). The influence coefficient for the source is

$$B_{JK} = \iint\limits_{\text{Panel K}} \frac{1}{r} dS \tag{13}$$

and

$$C_{JK} = \iint\limits_{\text{Panel K}} \vec{n} \cdot \nabla_K \left(\frac{1}{r} \right) dS \tag{14}$$

for the doublet.

The velocity-influence coefficients for the source and doublet are, respectively (ref. 9),

$$\vec{V}_{\sigma JK} = - \iint\limits_{\text{Panel K}} \nabla_J \left(\frac{1}{r} \right) dS \tag{15}$$

and

$$\vec{V}_{\mu_{JK}} = - \iint\limits_{\text{Panel K}} \nabla_J \left[\vec{n}_K \cdot \nabla_K \left(\frac{1}{r} \right) \right] dS \tag{16}$$

In PMARC, either the Dirichlet or Neumann boundary conditions can be applied to the surface panels, and a combination of the two can be applied to a given geometry. Equation (11) is applied if the designated patch (a group of panels) is part of a thick boundary enclosing an inner volume. This type of patch is called a Dirichlet patch. A form of equation (12), where only the induced normal velocities are considered, is used if the patch is part of an open surface. This type of patch is called a Neumann patch (ref. 9).

The remaining discussion will focus on the solution of the velocity equation (12). The solution technique involves finding the velocity contribution from the doublet and source of each panel. The total contribution is the sum of all the panels. The induced velocity at a point P by a constant unit strength doublet distribution over a panel is given by equation (16). Using the vector identity

$$\vec{a}(\vec{b} \cdot \vec{c}) = (\vec{a} \times \vec{b}) \times \vec{c} + \vec{b}(\vec{a} \cdot \vec{c})$$

equation (16) becomes

$$V_{\mu_{JK}} = -\iint\limits_{\text{Panel K}} \left\{ (\vec{n} \times \nabla_J) \times \nabla_K\left(\frac{1}{r}\right) + \vec{n}\left[\nabla_J \cdot \nabla_K\left(\frac{1}{r}\right)\right]\right\} dS \tag{17}$$

Noting that

$$\nabla_K\left(\frac{1}{r}\right) = -\nabla_J\left(\frac{1}{r}\right)$$

and remembering that potential flow satisfies Laplace's equation, equation (17) further reduces to

$$V_{\mu_{JK}} = -\iint\limits_{\text{Panel K}} (\vec{n} \times \nabla_J) \times \nabla_K\left(\frac{1}{r}\right) dS \tag{18}$$

or

$$V_{\mu_{JK}} = -\iint\limits_{\text{Panel K}} (\vec{n} \times \nabla_J) dS \times \nabla_K\left(\frac{1}{r}\right) \tag{19}$$

By applying the identity

$$\iint\limits_{S} (\vec{n} \times \nabla) dS = \oint_C d\vec{r}$$

equation (19) can be rewritten as

$$V_{\mu_{JK}} = -\oint d\vec{s} \times \nabla\left(\frac{1}{r}\right) \tag{20}$$

but

$$\nabla_K\left(\frac{1}{r}\right) = -\nabla_J\left(\frac{1}{r}\right) = -\frac{\vec{r}}{r^3} \tag{21}$$

Finally, the velocity at any point P due to constant doublet distribution over a panel is given by

$$V_{\mu_{JK}} = -\oint \frac{\vec{r} \times d\vec{s}}{r^3} \tag{22}$$

This is the Biot-Savart equation for the velocity induced at a point by a line vortex.

The line integral of equation (22) is solved by considering only one side of a panel at a time. The total contribution from the panel is the sum of the contributions of the four sides. The solution of equation (22) for one side of a panel is

$$V_{\mu_{JK}} = \frac{(\vec{a} \times \vec{b})\left|\vec{a} + \vec{b}\right|}{A(B)[(A)(B) - \vec{a} \cdot \vec{b}]} \tag{23}$$

where A and B are the magnitudes of $\vec{a}$ and $\vec{b}$ defined by figure 2.

If the point in question is far enough away from a panel, a far-field approximation can be made without significantly affecting the solution's accuracy. The approximation assumes that a doublet can be treated as a point doublet instead of a distributed doublet. This allows the integral to be replaced with the multiplication of the integrand and the panel area whose contribution is being evaluated. The same argument holds for the treatment of the source contribution. Assuming a unit doublet is used, the far-field expression is

$$V_{\mu_{JK}} = -\nabla_J\left[\vec{n} \cdot \nabla_K\left(\frac{1}{r}\right)\right]\text{area}_K \tag{24}$$

or

$$V_{\mu_{JK}} = -\nabla_J\left(\frac{\vec{n} \cdot \vec{r}}{r^3}\right)\text{area}_K \tag{25}$$

where r is the distance from the centroid of panel K to the influenced point.

The solution of this equation is

$$V_{\mu_{JK}} = -\text{area}_K \frac{-3(PN)\vec{r} + r^2\vec{n}}{r^5} \tag{26}$$

The completed proofs of equations (23) and (26) and the definition of PN are given in Appendix A.

The contribution to the induced velocity of a constant unit strength source distribution over a panel is given by equation (15). After substituting equation (21) into equation (15), it becomes

$$V_{\sigma_{JK}} = \iint_{\text{Panel K}} \frac{\vec{r}}{r^3} dS \tag{27}$$

The solution is

$$V_{\sigma_{JK}} = GL\left[(SM)(\vec{I}) - (SL)(\vec{M})\right] + C_{JK}\vec{n} \tag{28}$$

See Appendix B for the definitions of the nomenclature.

The far-field equation for the source of unit strength is simply

$$V_{\sigma_{JK}} = \text{area}_K\left(\frac{\vec{r}}{r^3}\right) \tag{29}$$

For the completed proofs see Appendix B.

It should be pointed out that although the doublet solution, equation (23), is valid for a twisted panel (a panel that is nonplanar), the source solution, equation (28) is not. This problem should not usually affect a particular geometry that may have a limited number of twisted panels because the far-field approximation is used about 90% of the time for most configurations. In some cases, however, a twisted panel may cause the doublet solution to converge slowly. This phenomenon is investigated in Appendix C.

Since the singularities are known from the doublet solution, the velocities on each control point can be evaluated (ref. 8). The tangential velocities are found by differentiating the doublet strengths in the appropriate directions, while the normal velocity is either zero or a user-defined value. From the resulting velocity at each control point the corresponding pressure coefficient is found by the equation

$$C_{P_K} = 1 - \frac{V_K^2}{V_\infty^2} \tag{30}$$

Finally, the lift and drag forces can be calculated by numerically integrating the pressure distribution, and the moment coefficients can be determined around a user-defined reference line.

2.1.1 Shortcomings of Potential Flow-Based Computer Codes– Because potential flow-based codes exclude viscous effects, they cannot predict friction drag. By assuming that a thin wake exists, the viscous wake blockage is reduced. This results in a decrease of the calculated drag on the computer model. Also, older panel codes could not accurately predict the shape of free wakes. PMARC improves this by taking into account the unsteady nature of the wake by using a time-stepping technique (ref. 10). Although the wake is still assumed to be thin, the new wake modeling will allow a more realistic wake roll-up calculation and improve the computational capability. Modeling of separated flow is also a problem for panel codes. One possible method for modeling the separation is for the user to attach a wake at a guessed separation line on the body and to enclose the end of the wake with the end of the trailing-edge wake. This model can help incorporate the effect of wake blockage into the computations. This technique, however, needs further study.

2.1.2 Method of Removing the Wind Tunnel Walls– Wind tunnel walls are removed by moving them far enough away from the tested body so they have little or no influence on it. Because it is important to retain the same matrix for the two computations, the integrity of the RHS of the doublet matrix equation is maintained by not removing the wind tunnel walls. Elimination of the tunnel walls from the model would result in a slight difference to the RHS which would result in a slightly different solution. The extent of the difference would depend on the individual case.

2.1.3 Calculation of the Wall Correction Factor– The correction factor is found by taking the ratio of the lift coefficients of the two computer model cases and applying it to the dynamic pressure such that (ref. 11)

$$\frac{q_c}{q_m} = \left(\frac{C_{L_w}}{C_{L_{nw}}}\right)_{\text{Calculated}} \tag{31}$$

To find the "corrected" dynamic pressure, q_c, the lift-coefficient ratio is simply multiplied by the measured dynamic pressure from the wind tunnel test, q_m. The corrected dynamic pressure can then be applied to the aerodynamic coefficient calculations to find the corrected force and moment coefficients.

3. DISCUSSION OF RESULTS

3.1 Case One: The Two-Dimensional High-Lift Wing

The two-dimensional test case was modeled after a wind tunnel test of a high-lift NACA 4412 airfoil equipped with a NACA 4415 single-slotted flap at the ARC 7- by 10-Foot Wind Tunnel (ref. 6). For the wind tunnel test, the chord length of the wing was 35 in. and 14 in. for the flap. The angle of attack was 8.2° and the flap deflection was 21.8°.

The two-dimensional characteristics of the wing and flap were modeled by extending their span to 1000 times the chord length of the wing. The upper and lower walls of the wind tunnel were modeled in the same manner. The side walls were not included in the computer model because they were not necessary because of the two-dimensionality of the problem. The pressures and forces on the walls and the airfoils were taken only from the center of the configuration to assure that they would not be skewed by tip effects. Figure 3 shows a section of the PMARC model.

3.1.1 Verification of the Computer Model– The first step was to estimate the distortion in the free stream resulting from the model blockage effects in the wind tunnel. This was done by examining the predicted velocity profile at the centerline of the test section near the location of the wind tunnel pitot tube. The velocity profile is presented in figure 4: The velocity profile does show a dynamic pressure increase which, as stated earlier, is caused by the blockage effects. Since no data from the experiment were available, this procedure was used only to validate that blockage effects were predicted by the computer model.

The next step was to compare the wall-pressure signature resulting from the model blockage effects in the test section. The comparison of the wall-pressure signatures from the wind tunnel test and the computations are shown in figure 5. The peak from the wall-pressure signature matched very well, thus giving confidence to the technique. The lower wall-pressure signatures, however, did not. One possible explanation (keeping in mind that the wind tunnel test was of a high-lift nature) is that a separation bubble occurred at the floor of the wind tunnel during the test. It would have resulted from the circulation caused by the wakes from the airfoils interacting with the boundary-layer separation from the floor, which the panel code would not have been able to predict. Another possible explanation is that the highly deflected flap wake interacted with the floor boundary layer, which, also, could not be modeled by PMARC. In either case, it is impossible to be certain because neither effect was observed during the experiment.

Another means of checking the validity of the panel model was to compare the pressure distributions over the wing and flap airfoils, as shown in figures 6 and 7, respectively. Included in the figures are the pressure distributions from the PMARC test case that did not include the tunnel walls. PMARC accurately predicted the pressure distribution over the wing. The discrepancy between the wind tunnel test data and the PMARC test data for the flap was attributed to the separation from the wing disrupting the flow over the flap. The large pressure peak at the leading edge of the flap was due to the high acceleration of the flow predicted by the code through the flap gap. This occurred because the panel code could not predict the viscous flow in the gap region. The wind tunnel test data also showed a separated wake coming off the last 30% of the flap, which PMARC did not predict.

Another approach taken to show that the panel code predicted the solid blockage effect was to move the wind tunnel walls away from the wing and flap to determine whether the solution of the lift and moment coefficients converged as the height between the airfoils and the tunnel walls increased. Figures 8 and 9 show the results from the investigation. As expected, the lift coefficient decreased for both the wing and the flap. This was a result of the decrease of the dynamic pressure over the configuration and it is an excellent example of the effect of solid blockage. The moment coefficient of the wing decreased as the walls were moved, but increased for the flap. The decrease in lift caused a decrease in the pitching moment and resulted in a lowering of the C_M of the wing. The effect on the flap would be explained by a broad distribution of the lift. In other words, the lift was not concentrated near the quarter chord because of a shift of the center of pressure. The result was that the lift was evenly distributed over the entire flap. Therefore, although the total lift coefficient decreased, the pitching moment coefficient increased as the tunnel walls were moved farther from the model. Again, a combined single correction for the solid and wake blockages is found by taking the percentage difference between the two cases, with and without the influence of the tunnel walls.

Other methods, however, calculate the solid blockage and wake blockage corrections separately. Keeping this in mind, matching the wing pressure distribution with the wind tunnel test gives credibility to the solid blockage effect being predicted correctly by PMARC. The interaction of the flow over the wing with the wind tunnel walls was responsible for the increase in dynamic pressure which is the solid blockage. The disparity of the pressure distribution over the flap between the PMARC test case and the wind tunnel test show that the PMARC model did not predict the wake blockage as accurately. This was due to a separated wake coming off the flap, which could not be modeled. It is difficult to determine whether this difference was appreciable because the corrections obtained from PMARC were similar to the corrections obtained using other methods (ref. 6).

3.1.2 Wall Correction Computed by PMARC– The total section lift data and the corresponding corrections from PMARC are tabulated in table 1. The data are taken from the five spanwise sections of the configuration. The coefficients were lower on the last section because of tip effects and because this was a three-dimensional effect, they were omitted from the correction calculations. Slight tip effects also caused minor increases in the coefficients farther out in the spanwise direction. The PMARC lift data compared favorably with the wind tunnel test lift data. The test measured a C_L of 3.2 (ref. 6) for the main wing, a 14% change compared with the PMARC test case. The difference can be attributed to the overprediction of the leading-edge pressure peak by PMARC. The overprediction is a characteristic of panel codes because they cannot predict the viscous flow that occurs at the leading edge of an airfoil.

TABLE 1.– COEFFICIENT OF LIFT CALCULATED BY PMARC

Section	With Tunnel Wall	Without Tunnel Walls	q_c/q_m
1	5.413	5.055	1.071
2	5.413	5.055	1.071
3	5.413	5.055	1.071
4	5.413	5.053	1.071
5	5.412	5.019	1.078

3.1.3 Wall Correction Comparison– The wall corrections were computed by four other methods and are tabulated in table 2. The six methods from reference 4 were of the same magnitude (the methods of Pope, Allen and Maskell and PMARC were almost identical). The methods of Allen and Maskell, Pope, and Thom were based on the classical approach outlined in the introduction. The equation used by Thom was a simplified form of Herriot's equations which predicted a higher correction than the others. Merker's was lower, but his method was originally developed for automotive wind tunnel testing.

TABLE 2.– WALL CORRECTION FACTORS
BY VARIOUS METHODS

Method	q_c/q_m
Allen and Maskell	1.072
Merker	1.046
PMARC	1.071
Pope	1.070
Thom	1.090

3.2 Case Two: The F/A-18 Aircraft Model

3.2.1 Model Fabrication and Wind Tunnel Apparatus– The F/A-18 aircraft test was conducted in the low-speed 32- by 45-in. closed-circuit wind tunnel at SDSU. The 1/32-scale model was manufactured by the Hasegawa Model Company of Japan and was reinforced internally with a steel frame, several balsa wood ribs, fiberglass, and epoxy so it would be structurally sound at high angles of attack. The model was 23.5 in. long with a wingspan of 14 in. and a mean aerodynamic chord of 4.32 in. The test was conducted with a 2.5-in. radar boom attached at the nose (without the wingtip missiles). Diagrams of the model and the test section are shown in figures 10 and 11, respectively. The model was connected to two fixed struts that were attached to the wings and an adjustable hinged jackscrew that was attached to the arresting hook underneath the tail section. The force and moment data were acquired using a six-component load balance in conjunction with a Hewlett-Packard Data Acquisition System. The static upper wall pressures were taken along the centerline of the tunnel using a differential water manometer board. The signature measurements extended from the plane of the pitot-static ports to downstream from the model but they were still within the test section as shown in figure 12.

3.2.2 Validation of the Wind Tunnel Test– The wind tunnel tests were conducted at varying dynamic pressures and angles which ranged from 16.4 to 36.9 lb/ft^2 and 1° to 56°, respectively. The dynamic pressures represented a range of velocities from 117 to 176 ft/sec, which resulted in Reynolds numbers between 242,000 and 364,000, based on the mean aerodynamic chord. The test angle range was chosen to serve a dual purpose. The first and foremost reason was to show the viability of the panel code wall correction method. The second was to determine the tunnel wall corrections that would be needed for a full-scale test at high angles of attack in the 40- by 80-Foot Wind tunnel at the National Full-Scale Aerodynamic Complex at ARC. The 1/32 model size was chosen because it allowed the opportunity to geometrically simulate such a test in the SDSU wind tunnel because the plane/wind tunnel test section area ratios were the same. Since a large amount of separation would most certainly occur at high angles of attack, the PMARC calculated wall corrections would only be a guideline for that wind tunnel test.

To determine whether the SDSU wind tunnel test data were accurate, the measured aerodynamic characteristics were compared with the results from reference 12. The comparison is presented in figure 13. The C_L and C_D data show a very good correlation between the two tests. From this comparison it was determined that the data obtained from the wind tunnel test were reasonably accurate such that valid wall corrections could be calculated.

3.2.3 Verification of the Computer Model– The PMARC F/A-18 computer model was modified from an existing data file generated by McDonnell Douglas which is presented in figure 14. The changes involved modifying the panel density of the wings and both stabilizers and eliminating the sharp edge created by the intersection of the ventral nacelles. The changes were made to eliminate solution convergence problems of the original McDonnell Douglas model. By smoothing out the sharp edges on the body and by eliminating the inconsistent paneling, a "cleaner" computer model was produced that did not have the convergence problems. The repaneled model is shown in figure 15. The finished model was not as detailed as the original, but because the only concern was the blockage effects, it was considered an acceptable tradeoff.

The geometry went through three derivations before the final configuration of 1336 panels was settled upon. Problems occurred at the intersection of the the wing and the horizontal and vertical tails which resulted in a couple of slightly twisted panels on the main fuselage near the trailing edge of the wing which caused the solution to converge slowly. The upper wall-pressure distribution was used to validate the computer solution. The comparisons of the wind tunnel and PMARC signatures are presented in figure 16. They do not compare as favorably as the two-dimensional airfoil. The trends were the same; however, the magnitudes were not. The wind tunnel test pressure coefficient peaks were about 20% larger for the 46° and 20° cases and as much as 80% larger between the 0° (the PMARC model) and the 1° (the wind tunnel test) case. These results indicate that the computer model was not creating as much blockage as the wind tunnel model.

The C_L of the F/A-18 computer model was affected by the placement of the wakes. Originally, the wakes extended from the trailing edges of the wing and the horizontal and vertical tails and were allowed to follow the path of the free stream. At low angles of attack, however, the C_L was higher without the influence of the wind tunnel walls than with the walls' influence. It was obvious that the computer model was in error. After remodeling the aircraft it was discovered that the problem was with the placement of the wakes. By allowing the wing wake to follow the free stream, it cut through the vertical tail and caused an excessive amount of drag on the aircraft. The problem was solved by manually forcing the wing wake around the vertical tail. Also, instead of the wakes immediately following the path of the free stream, they were forced to follow the aircraft's angle of attack for a distance half the length of the plane before they turned in the direction of the free stream. The distance the wake followed the aircraft's angle of attack was determined after manipulating many different test cases. It was discovered during this time that an endless variety of lift data within a 10% margin could be generated depending on the placement of the wake. The best course was to place the wake where it would be expected during a wind tunnel test. It must be pointed out that the wake must be placed in the same location for both computer calculations. After the adjustments to the wakes were made, the C_L data and the wall corrections at all angles of attack were more believable. The predicted aerodynamic characteristics are presented in figure 13.

3.2.4 Wall Corrections Computed by PMARC– Before discovering that the wake placement was causing most of the problems with the computer model, a study was conducted to determine whether the wing of the F/A-18 model, figure 17, followed the same C_L trend as the full configuration. The wing was found to follow the expected trend, which led the troubleshooting in the direction of the wake problem. The correction data for the wing and the full configuration are presented, with other correction techniques, in figure 18. It can be seen from figure 18 that the panel code correction method predicted wall corrections similar to the classical methods. The conclusion, therefore, is that the technique was successful in adequately predicting the wall corrections for the F/A-18.

4. CONCLUSIONS

A study was conducted to determine the viability of using a low-order panel code to calculate wind tunnel wall corrections. Results of the investigation were promising. The panel code, PMARC, predicted the dynamic pressure wall correction for a two-dimensional airfoil to be 1.071, which was similar to the wall correction prediction made by other techniques. Although the flow separation that occurred during the wind tunnel test could not be modeled by PMARC, the wall correction was not significantly affected. The prediction of the F/A-18 aircraft wall corrections posed other challenges and problems, of which the geometry development and wake placement were the most serious. The geometry generation was a challenge because of its complexity, and the variety of the wake placement was a problem because it severely affected the wall correction. Eventually, the problems were satisfactorily resolved so that the final results compared favorably with other methods.

Although many problems occurred during this study, much insight was gained into the use of panel codes as a means of predicting wind tunnel wall corrections. It was evident that to use this technique effectively, care must be taken during the generation of complex geometries and when choosing the proper wake placements. In the future, it is hoped that improved separation and boundary-layer modeling techniques will be developed. When this is accomplished, the accuracy of wind tunnel wall corrections for complex geometries determined by panel codes will greatly improve.

PRECEDING PAGE BLANK NOT FILMED

PAGE 16 INTENTIONALLY BLANK

APPENDIX A

SOLUTION OF THE DOUBLET CONTRIBUTION TO THE INDUCED VELOCITY

An introductory phase of this research project was to study the structure of first-order panel codes. For this study the influence coefficients were analyzed first and then the formulation was numerically investigated. In Appendices A and B the mathematical formulations are provided, and in Appendix C the numerical influence of these elements will be investigated.

Starting with the Biot-Savart equation,

$$V_{\mu_{JK}} = -\oint \frac{\vec{r} \times d\vec{s}}{r^3} \tag{A1}$$

By considering only one side of a panel, the line integral can be changed to a single-element integral. Now, let $\vec{e}$ represent the direction formed by $\vec{r} \times d\vec{s}$ such that

$$\vec{r} \times d\vec{s} = -\vec{e} r \sin\theta \, ds \tag{A2}$$

From figure 19

$$r = \frac{h}{\sin\theta} \tag{A3}$$

and

$$s = \frac{h}{\tan\theta} \tag{A4}$$

which results in

$$ds = \left(\frac{h}{\sin^2\theta}\right) d\theta \tag{A5}$$

Substituting in equation (A2) and equation (A5), equation (A1) becomes

PRECEDING PAGE BLANK NOT FILMED

PAGE 18 INTENTIONALLY BLANK

$$V_{\mu_{JK}} = -\int_{\theta_1}^{\theta_2} \frac{\vec{e}(h/\sin\theta)\sin\theta(h/\sin^2\theta)d\theta}{\left(h^3/\sin^3\theta\right)} = -\frac{\vec{e}}{h}\int_{\theta_1}^{\theta_2} \sin\theta\, d\theta = -\frac{\vec{e}}{h}[-\cos\theta]_{\theta_1}^{\theta_2} = -\frac{\vec{e}}{h}[\cos\theta_1 - \cos\theta_2] \quad \text{(A6)}$$

From figure 19

$$\cos\theta_1 = \frac{\left(\vec{a}-\vec{b}\right)\cdot\vec{a}}{\left|\vec{a}-\vec{b}\right|\left|\vec{b}\right|} \quad \text{(A7)}$$

$$\cos\theta_2 = \frac{(\vec{a}-\vec{b})\cdot\vec{b}}{\left|\vec{a}-\vec{b}\right|\left|\vec{b}\right|} \quad \text{(A8)}$$

Substituting equations (A7) and (A8) into equation (A6)

$$\cos\theta_1 - \cos\theta_2 = \frac{(\vec{a}-\vec{b})\cdot\vec{a}}{\left|\vec{a}-\vec{b}\right|\left|\vec{a}\right|} - \frac{(\vec{a}-\vec{b})\cdot\vec{b}}{\left|\vec{a}-\vec{b}\right|\left|\vec{b}\right|} = \frac{1}{\left|\vec{a}-\vec{b}\right|}\left[\frac{(\vec{a}-\vec{b})\cdot\vec{a}}{\left|\vec{a}\right|} - \frac{(\vec{a}-\vec{b})\cdot\vec{b}}{\left|\vec{b}\right|}\right]$$

$$= \frac{1}{\left|\vec{a}-\vec{b}\right|}\left[\frac{\vec{a}\cdot\vec{a}-\vec{a}\cdot\vec{b}}{\left|\vec{a}\right|} - \frac{\vec{a}\cdot\vec{b}-\vec{b}\cdot\vec{b}}{\left|\vec{b}\right|}\right] = \frac{1}{\left|\vec{a}-\vec{b}\right|}\left[\left|\vec{a}\right| - \frac{\vec{a}\cdot\vec{b}}{\left|\vec{a}\right|} - \frac{\vec{a}\cdot\vec{b}}{\left|\vec{b}\right|} + \left|\vec{b}\right|\right]$$

$$= \frac{1}{\left|\vec{a}-\vec{b}\right|}\left|\left|\vec{a}\right| + \left|\vec{b}\right| - \frac{\left(\left|\vec{a}\right| + \left|\vec{b}\right|\right)\left(\vec{a}\cdot\vec{b}\right)}{\left|\vec{a}\right|\left|\vec{b}\right|}\right| = \frac{\left|\vec{a}\right| + \left|\vec{b}\right|}{\left|\vec{a}-\vec{b}\right|}\left|1 - \frac{\vec{a}\cdot\vec{b}}{\left|\vec{a}\right|\left|\vec{b}\right|}\right| = \frac{A+B}{\left|\vec{a}-\vec{b}\right|}\left[\frac{A*B-\vec{a}\cdot\vec{b}}{A*B}\right] \quad \text{(A9)}$$

$\vec{e}$= unit vector between $\vec{a}$ and $\vec{a}-\vec{b}$

$$\vec{e} = \frac{\left(\vec{a}\times\left(\vec{a}-\vec{b}\right)\right)}{\left|\vec{a}\times\left(\vec{a}-\vec{b}\right)\right|} = \frac{\left(\vec{a}\times\vec{a}-\vec{a}\times\vec{b}\right)}{\left|\vec{a}\times\vec{a}-\vec{a}\times\vec{b}\right|} = -\frac{\vec{a}\times\vec{b}}{\left|\vec{a}\times\vec{b}\right|} \quad \text{(A10)}$$

The perpendicular distance h is

$$h = \frac{1}{\left|\vec{a}\times\vec{b}\right|}\left|(\vec{a}-\vec{b})\times\vec{a}\right| = \frac{\left|\vec{a}\times\vec{b}-\vec{a}\times\vec{a}\right|}{\left|\vec{a}-\vec{b}\right|} = \frac{\left|\vec{a}\times\vec{b}\right|}{\left|\vec{a}-\vec{b}\right|} \quad \text{(A11)}$$

Substituting equations (A9), (A10), and (A11) into equation (A6) yields

$$V_{\mu_{JK}} = -\left[-\frac{\left(\vec{a}\times\vec{b}\right)\left|\vec{a}-\vec{b}\right|}{\left|\vec{a}\times\vec{b}\right|\left|\vec{a}\times\vec{b}\right|}\right]\frac{A+B}{\left|\vec{a}-\vec{b}\right|}\left[\frac{A*B-\vec{a}\cdot\vec{b}}{A*B}\right] = \frac{\left(\vec{a}\times\vec{b}\right)}{\left|\vec{a}\times\vec{b}\right|^{2}}(A+B)\left[\frac{A*B-\vec{a}\cdot\vec{b}}{A*B}\right] \tag{A12}$$

And finally,

$$V_{\mu_{JK}} = \frac{\left(\vec{a}\times\vec{b}\right)(A+B)}{A*B*\left(A*B-\vec{a}\cdot\vec{b}\right)} \tag{A13}$$

The point doublet is simply the integrand from the general solution multiplied by the panel area.

$$V_{\mu_{JK}} = -\nabla_{J}\left[\vec{n}\cdot\nabla\left(\frac{1}{r}\right)\right]*\text{area}_{K} = -\text{area}_{K}*\nabla_{J}\left(\frac{\vec{n}\cdot\vec{r}}{r^{3}}\right) \tag{A14}$$

Letting

$$\vec{n} = \langle 0,0,1\rangle$$

$$\vec{r} = \langle l,m,n\rangle$$

results in

$$\vec{n}\cdot\vec{r} = n$$

$$r^{3} = (l^{2}+m^{2}+n^{2})^{3/2}$$

thus

$$\nabla_J\left(\frac{\vec{n}\cdot\vec{r}}{r^3}\right) = \nabla_J\left(\frac{n}{\left(l^2+m^2+n^2\right)^{3/2}}\right)$$

$$= -\frac{3}{2}\left[\frac{2ln}{\left(l^2+m^2+n^2\right)^{5/2}}\right]\vec{i} - \frac{3}{2}\left[\frac{2mn}{\left(l^2+m^2+n^2\right)^{5/2}}\right]\vec{j} - \frac{3}{2}\left[\frac{2n^2}{\left(l^2+m^2+n^2\right)^{5/2}}\right]\vec{k}$$

$$= -\left[\frac{1}{\left(l^2+m^2+n^2\right)^{5/2}}\right]\vec{k} - 3\left[\frac{n\left(l\vec{i}+m\vec{j}+n\vec{k}\right)}{(l^2+m^2+n^2)^{5/2}}\right] + \left[\frac{l^2+m^2+n^2}{\left(l^2+m^2+n^2\right)^{5/2}}\right]\vec{k}$$

$$= \frac{-3*PN*\vec{r}+r^2*\vec{n}}{r^5} \qquad \text{(A15)}$$

where, from figure 20,

$$PN = \frac{n}{\left(l^2+m^2+n^2\right)^{3/2}}$$

Finally,

$$V_{\mu_{JK}} = \text{area}_k \frac{3*PN*\vec{r}+r^2*\vec{n}}{r^5} \qquad \text{(A16)}$$

APPENDIX B

SOLUTION OF THE SOURCE CONTRIBUTION TO THE INDUCED VELOCITY

The source potential is solved by the technique presented by Hess (ref. 13). From the potential

$$B_{JK} = \iint\limits_{\text{Panel},K} \frac{1}{r} dS \tag{Bl}$$

where

$$r = \sqrt{R^2 + Z^2}$$

$$R = (x - \varepsilon)^2 + (y - \eta)^2$$

$$dS = R * dR * d\theta$$

Rewriting equation (B1),

$$B_{JK} = \oint \int_0^R \frac{RdR}{\sqrt{R^2 + Z^2}} d\theta$$

But

$$r = \sqrt{R^2 + Z^2}$$

$$dr = \frac{RdR}{\sqrt{R^2 + Z^2}}$$

The integral now becomes

$$B_{JK} = \oint \left[\int_{|Z|}^{r} dr \right] d\theta = \oint (r - |Z|) d\theta = \oint r d\theta - |Z| \Delta\theta \tag{B2}$$

Realizing that R and Z represent the parallel and normal planes, where $Z = 0$ and $x = y = 0$, respectively, the integral from equation (B2) can be written

$$\oint r d\theta = \oint R d\theta + \oint Z d\theta$$

If the integrals are solved for just one side of the panel, the line integral disappears and

$$\int r d\theta = \int R d\theta + \int Z d\theta \tag{B3}$$

To solve the integrals it is necessary to define the following quantities. The directional unit vectors for the problem are, from figure 21

$$\vec{l} = \frac{x-\varepsilon}{\sqrt{R^2+Z^2}}$$

$$\vec{m} = \frac{y-\eta}{\sqrt{R^2+Z^2}}$$

$$\vec{n} = \frac{Z}{\sqrt{R^2+Z^2}}$$

From figure 22,

$$|d| = \sqrt{(\varepsilon_2-\varepsilon_1)+(\eta_2-\eta_1)}$$

$$\cos\alpha = \frac{(\varepsilon_2-\varepsilon_1)}{d}$$

$$\sin\alpha = \frac{(\eta_2-\eta_1)}{d}$$

where

$$\frac{\vec{d}}{|\vec{d}|} = \langle \cos\alpha, \sin\alpha, 0 \rangle$$

$$\vec{R} = \langle \varepsilon - x, \eta - y, 0 \rangle$$

$$R_1 = \langle \varepsilon_1 - x, \eta_1 - y, 0 \rangle$$

$$R_2 = \langle \varepsilon_2 - x, \eta_2 - y, 0 \rangle$$

and

$$S = (\varepsilon - x)\cos\alpha + (\eta - y)\sin\alpha$$

$$S_1 = (\varepsilon_1 - x)\cos\alpha + (\eta_1 - y)\sin\alpha$$

$$S_2 = (\varepsilon_2 - x)\cos\alpha + (\eta_2 - y)\sin\alpha$$

The perpendicular distance from the vector $\vec{d}$ to the point defined by (x,y,0) is

$$R_{12} = \frac{\vec{d} \times \vec{R}}{|\vec{d}|} = (x - \varepsilon_1)\sin\alpha - (y - \eta_1)\cos\alpha = (x - \varepsilon_2)\sin\alpha - (y - \eta_2)\cos\alpha$$

The solution for the first term of equation (B4) is, noting that

$$R^2 = S^2 + R_{12}^2$$

$$S^2 = R^2 - R_{12}^2$$

$$\cos\theta = \frac{R_{12}}{R}$$

$$\sin\theta = \frac{S}{R} = \frac{\sqrt{R^2 - R_{12}^2}}{R}$$

and differentiating

$$d\theta(\cos\theta) = \left[-\frac{\left(R^2 - R_{12}^2\right)^{1/2}}{R^2} + \frac{(1/2)(2R)}{R\left(R^2 - R_{12}^2\right)^{1/2}} \right] dR$$

$$d\theta = \frac{1}{\cos\theta} \left[\frac{\left(R^2 - R_{12}^2\right)^{1/2} \left(R^2 - R_{12}^2\right)^{1/2} + R^2}{R^2 \left(R^2 - R_{12}^2\right)^{1/2}} \right] dR$$

$$d\theta = \frac{R}{R_{12}} \left[\frac{R_{12}^2}{R^2 \left(R^2 - R_{12}^2\right)^{1/2}} \right] dR = \frac{R_{12}\, dR}{R\left(R^2 - R_{12}^2\right)^{1/2}}$$

thus

$$\int R d\theta = \int_{R_1}^{R_2} \frac{R * R_{12} dR}{R\left(R^2 - R_{12}^2\right)^{1/2}} = R_{12} \int_{R_1}^{R_2} \frac{dR}{\left(R^2 - R_{12}^2\right)^{1/2}}$$

$$= R_{12}\left[\log(R_2 + \sqrt{R_2^2 - R_{12}^2}) - \log(R_1 + \sqrt{R_1^2 - R_{12}^2})\right]$$

but

$$S_1 = \sqrt{R_1^2 - R_{12}^2}$$

$$S_2 = \sqrt{R_2^2 - R_{12}^2}$$

Finally,

$$\int R d\theta = R_{12}\left[\log(R_2 + S_2) - \log(R_1 + S_1)\right] = R_{12} \log\left|\frac{R_2 + S_2}{R_1 + S_1}\right|$$

This equation can be rewritten as

$$\int R d\theta = R_{12} \log\left|\frac{R_1 + R_2 + d}{R_1 + R_2 - d}\right| \qquad \text{(B4)}$$

The second term solution is simply

$$\int Z d\theta = Z \int_{\theta_1}^{\theta_2} d\theta = Z(\theta_2 - \theta_1)$$

Translating θ from the l and m plane to the normal plane

$$\theta_1 = \tan^{-1}\left(\frac{S_1}{R_{12}} |\vec{n}|\right)$$

$$\theta_2 = \tan^{-1}\left(\frac{S_2}{R_{12}} |\vec{n}|\right)$$

Thus

$$Z\int d\theta = \tan^{-1}\left(\frac{S_2 Z}{R_{12}R_2}\right) - \tan^{-1}\left(\frac{S_1 Z}{R_{12}R_1}\right)$$

But from the trigonometry identity,

$$\tan^{-1}\left(\frac{A}{B}\right) - \tan^{-1}\left(\frac{C}{D}\right) = \tan^{-1}\left(\frac{AD - BC}{BD + AC}\right)$$

$$Z\int d\theta = Z * \tan^{-1}\left(\frac{Z * R_{12}(R_1 S_2 - R_2 S_1)}{\left(R_{12}^2 R_1 R_2 + Z^2 S_1 S_2\right)}\right) \tag{B5}$$

The induced velocities are found by differentiating the potential, which yields for one side of a panel (ref. 13)

$$V_x = -\frac{\partial B_{JK}}{\partial x} = \cos\alpha * R_{12} \log\left|\frac{R_1 + R_2 + d}{R_1 + R_2 - d}\right| \tag{B6a}$$

$$V_y = -\frac{\partial B_{JK}}{\partial y} = \sin\alpha * R_{12} \log\left|\frac{R_1 + R_2 + d}{R_1 + R_2 - d}\right| \tag{B6b}$$

$$V_Z = -\frac{\partial B_{JK}}{\partial Z} = Z * \tan^{-1}\left(\frac{Z * R_{12}(R_1 S_2 - R_2 S_1)}{\left(R_{12}^2 R_1 R_2 + Z^2 S_1 S_2\right)}\right) \tag{B6c}$$

The total velocity influence is found by summing the contributions from the four sides of the panel.

PMARC uses the nomenclature developed for the panel code VSAREO (ref. 9) which is different from the Hess nomenclature. The method of solving the problem in the VSAERO nomenclature was not clear until the Hess solution was developed. The conversion from Hess to VSAERO follows.

Nomenclature from VSAERO:

$$C_{Jk} = \tan^{-1}\left[\frac{RNUM}{DNUM}\right]$$

$$RNUM = SM*PN*(B*PA - A*PB)$$

$$DNOM = PA*PB + PN^2 A*B*SM^2$$

$$PN = P_{JK} \cdot n$$

$$A = |\vec{a}|$$

$$B = |\vec{b}|$$

$$S = |\vec{s}|$$

$$PA = PN^2 SL + Al*AM$$

$$PB = PA - Al*SM$$

$$SM = \vec{s} \cdot \vec{m}$$

$$SL = \vec{s}*\vec{l}$$

$$AM = \vec{a} \cdot \vec{m}$$

$$AL = \vec{a} \cdot \vec{l}$$

$$Al = AM*SL - Al*SM$$

$$GL = \frac{1}{S}\log\left|\frac{A+B+S}{A+B-S}\right|$$

TABLE 3.– CONVERSION FROM THE HESS
TO THE VSAERO NOMENCLATURE

HESS	VSAERO
l, m, n	l, m ,n
R_1	$A = \lvert(AL, AM)\rvert$[a]
R_2	B
$\vec{\alpha} = (\sin\alpha * R_{12}, \cos\alpha * R_{12})$	$\vec{S} = (SL, SM)$[a]
$\vec{d} \times \vec{R}$	AM*SL – AL*SM
$Z * S_2$	PB
$Z * S_1$	PA
$Z * R_{12}(R_1 * S_2 - R_2 * S_1)$	RNUM
$Z * S_1 * S_2 + R_{12}^2 * R_1 * R_2$	DNOM

[a]The components are in the panel plane.

The final VSAERO form is

$$V_{\sigma_{JK}} = GL(SM * \vec{l} - SL * \vec{m}) + C_{JK}\vec{n} \tag{B7}$$

The point solution is

$$V_{\sigma_{JK}} = \text{area}_K \frac{\vec{r}}{r^3} \tag{B8}$$

APPENDIX C

PANEL ANALYSIS

For this panel analysis, the program PANEL.ANY (see the following section) was developed. The program was designed to find the induced velocity at an arbitrary point in space due to the influence of a uniform distribution of doublets and sources over a given panel. The investigation was done in three parts. The first part was to determine at what point the far-field approximation, based on the panel chord length, could be implemented. This was important because the computer time needed to calculate the far-field approximation was 40 times faster than the full integration technique. Considering that most problems consist of thousands of panels, and that the contribution from each panel must be calculated, it was evident that the approximation was important to the overall efficiency of the panel code. The second and third parts of the analysis were performed to determine the magnitude of the induced velocity at different locations from a uniform doublet and source distribution over a planar and twisted (nonplanar) panel, respectively. This analysis was important in understanding how the integration solution differed from the far-field point solution from different locations.

The first task was accomplished by using the program to choose an arbitrary point in space. The program calculated the induced velocity at that point by both the integral and the point methods. The program then formed a line between the chosen point and the center of the panel. The line was divided into 15 separate points and the program calculated the induced velocities at each point. A far-field radius was found by comparing the divergence between the point calculation and the more accurate integral formulation. The radius was the distance where the difference between the two methods was not appreciable. Many different initial point locations were tested during the analysis. After some trial and error, it was determined that a good starting radius was six panel chord lengths away from the center of the rectangular panel, with the chord length of the panel equaling unity. Three of the test cases are presented here.

The first case was a point directly above the center of the panel. For the second case the point was located over the median of the panel (fig. 23), where DW = 45°. For the last case the point was over the horizontal of the panel (fig. 24), where DW = 20°. The magnitude of the vector R, as stated earlier, was six panel chord lengths away from the center of the panel. Figures 25, 26, and 27 show the results from the three cases, respectively. The divergence of the first case occurred at the point farthest away from the panel at a radius of 2. The other two cases began their divergence closer to a radius of 1.6. From the other test cases not presented here, the worst divergence also occurred near a radius of 2. Allowing for some margin of safety, the far-field radius for the point solutions was finally determined to be 2.5.

The next task was the evaluation of the induced velocity as a line traversed over the panel. The user chose an initial point to begin the traverse either over the median, the horizontal, or a distance off the median of the panel (figs. 28 and 29). As before, the line was divided into 15 separate points. Except, in this case, the height above the panel remained constant. From figures 30 and 31, it is seen that the induced velocity of a line of points over the median and the horizontal of the panel were exactly the same for both the integral and point source methods. For this case the line was at a height of one panel chord length. The off-median case showed the same behavior. For this particular comparison the far-

PRECEDING PAGE BLANK NOT FILMED

PAGE 30 INTENTIONALLY BLANK

field factor was not important because only the difference made by the location of the line of points was studied.

The last task was to investigate the effect of a twisted panel on the induced velocities. As stated earlier, the doublet integral solution was not affected by a twisted panel because it treated the sides of a panel as line vortices. For this reason it was not studied. Thus, only the source solutions are presented here. Figure 32 shows the geometry of the twisted panel. For the test cases the height was one radius measured from the panel center and the line of points traversed the up diagonal of the panel. Results from twist angles (TW) of 0°, 10°, and 20° are shown in figures 33, 34, and 35, respectively. The integral solution was affected by the twisted panel; however, the point solution was not. At this time, no explanation can be found for the behavior of the integral solution.

The study was concluded by examining the influence of points of an off-median line over a twisted panel in which TW = 10°. Two cases were considered. The first was an off-median line that fell directly over the panel at DM = 0.25. The results are shown in figure 36. The only significant difference between the point and integral solutions was a slight phase shift. The second case considered a line that did not fall over the panel at DM = 3. The interesting results of this case are shown in figure 37. Again, no explanation can be offered. A further thorough analysis of the mathematics involved with the source integral solution will be necessary to answer the questions that resulted from this study.

C.1 The PANEL.ANY Program

```
C     PROGRAM PANEL.ANY

      DIMENSION X(5),Y(5),Z(5)

      PI=3.14159

      EPS=1.E-06

      THE45=SQRT(2.)/2.

      DUB=1.0

      SIG=1.0

      T=0.0

      CINC=0.0

      OPEN(2,FILE='INDIV',STATUS='NEW')

1     CONTINUE

C ***********************************************
```

```
C CASE ONE: MEDIAN        ***
C CASE TWO: OVER CORNER          ***
C CASE THREE: STRAIGHT LINE OVER MEDIAN    ***
C CASE FOUR: STRAIGHT LINE OVER HORIZONTAL    ***
C CASE FIVE: CHOOSE INITIAL POINT        ***
C **************************************************
   WRITE(6,*)'ENTER CASE AND TWIST(DEG):'
   READ(5,*) LLL,TW
   TW=TW*PI/180.
   X(1)=-.5
   X(2)=.5
   X(3)=.5
   X(4)=-.5
   Y(1)=-.5
   Y(2)=-.5
   Y(3)=.5
   Y(4)=.5

   DZ=TAN(TW)
   IF(DZ.GT.0.0)THEN
      Z(1)=DZ
      Z(2)=-DZ
      Z(3)=DZ
```

```
     Z(4)=-DZ
  ELSE
     DO 5 I=1,4
        Z(I)=0.0
5       CONTINUE
  ENDIF
  X(5)=X(1)
  Y(5)=Y(1)
  Z(5)=Z(1)
  IF(LLL.LE.2)THEN
     WRITE(6,*)'ENTER ANGLE:'
     READ(5,*) THETA
     THETA=THETA*PI/180.
     WRITE(6,*)'ENTER INCREMENT:'
     READ(5,*) TTT
  ELSE
     IF(LLL.EQ.5)THEN
        WRITE(6,*)'ENTER THE POINT LOCATION OF INTEREST:'
        READ(5,*) PXI,PYI,PZI
        WRITE(6,*)'ENTER INCREMENT:'
        READ(5,*) TTT
        GO TO 7
     ENDIF
     WRITE(6,*) 'ENTER OFF CENTERLINE INCREMENT:'
     READ(5,*) CINC
   ENDIF
   CALL CASE(LLL,PI,THETA,THE45,DI,PXI,PYI,PZI)
   T1XY=SQRT(PXI*PXI+PYI*PYI)/15.
7    CONTINUE
   DO 100 NT=1,31
     T=T+1.
     TT=T*TTT
     IF(LLL.LE.2.OR.LLL.EQ.5)THEN
       PX=PXI*TT
       PY=PYI*TT
       PZ=PZI*TT
     ELSE
       IF(LLL.EQ.3)THEN
         PX=PXI-(T-1.)*(PXI/15.)
         PY=PYI + CINC
         PZ=PZI
       ENDIF
       IF(LLL.EQ.4)THEN
         PX=(PXI-((T-1.)*T1XY/SQRT(2.))) +(CINC*THE45)
         PY=(PYI-((T-1.)*T1XY/SQRT(2.))) + (CINC*THE45)
         PZ=PZI
   ENDIF
ENDIF


RDIST=SQRT(PX*PX+PY*PY+PZ*PZ)
VX=0.0
VY=0.0
VZ=0.0
VXS=0.0
VYS=0.0
VZS=0.0
VXD=0.0
VYD=0.0
VZD=0.0
PVXS=0.0
PVYS=0.0
PVZS=0.0
PVXD=0.0
PVYD=0.0
PVZD=0.0
PNLX=.25*(X(1)+X(2)+X(3)+X(4))
PNLY=.25*(Y(1)+Y(2)+Y(3)+Y(4))
PNLZ=.25*(Z(1)+Z(2)+Z(3)+Z(4))
PNX=PX-PNLX
```

```
PNY=PY-PNLY

PNZ=PZ-PNLZ

PNS=SQRT(PNX*PNX+PNY*PNY+PNZ*PNZ)

D1X=X(3)-X(1)

D1Y=Y(3)-Y(1)

D1Z=Z(3)-Z(1)

D2X=X(4)-X(2)

D2Y=Y(4)-Y(2)

D2Z=Z(4)-Z(2)

CRX=D1Y*D2Z-D2Y*D1Z

CRY=D2X*D1Z-D1X*D2Z

CRZ=D1X*D2Y-D2X*D1Y

CRSQ=SQRT(CRX*CRX+CRY*CRY+CRZ*CRZ)

AREA=CRSQ/2.

CNX=CRX/CRSQ

CNY=CRY/CRSQ

CNZ=CRZ/CRSQ

PNN=CNX*PNX+CNY*PNY+CNZ*PNZ

TCMX=(X(3)+X(4))/2. - PNLX

TCMY=(Y(3)+Y(4))/2. - PNLY

TCMZ=(Z(3)+Z(4))/2. - PNLZ

TMS=SQRT(TCMX*TCMX+TCMY*TCMY+TCMZ*TCMZ)

CMX=((X(3)+X(4))/2. - PNLX)/TMS
```

```
CMY=((Y(3)+Y(4))/2. - PNLY)/TMS

CMZ=((Z(3)+Z(4))/2. - PNLZ)/TMS

CLX=CMY*CNZ-CNY*CMZ

CLY=CNX*CMZ-CMX*CNZ

CLZ=CMX*CNY-CNX*CMY

PVXD=AREA*(3.*PNN*PNX-PNS*PNS*CNX)/(PNS**5)

PVYD=AREA*(3.*PNN*PNY-PNS*PNS*CNY)/(PNS**5)

PVZD=AREA*(3.*PNN*PNZ-PNS*PNS*CNZ)/(PNS**5)

PVXS=AREA*PNX/(PNS**3)

PVYS=AREA*PNY/(PNS**3)

PVZS=AREA*PNZ/(PNS**3)


DO 20 J=1,4

   K=J+1

   AX=PX-X(J)

   AY=PY-Y(J)

   AZ=PZ-Z(J)

   BX=PX-X(K)

   BY=PY-Y(K)

   BZ=PZ-Z(K)

   SX=X(K)-X(J)

   SY=Y(K)-Y(J)

   SZ=Z(K)-Z(J)
```

```
      A=SQRT(AX*AX + AY*AY + AZ*AZ)

      B=SQRT(BX*BX + BY*BY + BZ*BZ)

      S=SQRT(SX*SX + SY*SY + SZ*SZ)

C SOURCE CONTRIBUTION

      SM=SX*CMX+SY*CMY+SZ*CMZ

      SL=SX*CLX+SY*CLY+SZ*CLZ

      AM=AX*CMX+AY*CMY+AZ*CMZ

      AL=AX*CLX+AY*CLY+AZ*CLZ

      BM=BX*CMX+BY*CMY+BZ*CMZ

      ALL=AM*SL-AL*SM

      RJ3=alog((A+B+S)/(A+B-S))/S

      PA=PNZ*PNZ*SL + ALL*AM

      PB=PA - ALL*SM

      RNUM=SM*PNZ*(B*PA - A*PB)

      DNOM=PA*PB + PNZ*PNZ*A*B*SM*SM

      DE=ATAN2(RNUM,DNOM)

      VXS=VXS+RJ3*(SM*CLX-SL*CMX)+DE*CNX

      VYS=VYS-(RJ3*(SM*CLY-SL*CMY)+DE*CNY)

      VZS=VZS+RJ3*(SM*CLZ-SL*CMZ)+DE*CNZ

C DOUBLET CONTRIBUTION

      AVBX=AY*BZ - AZ*BY

      AVBY=AZ*BX - AX*BZ

      AVBZ=AX*BY - AY*BX
```

```
         ADB=AX*BX + AY*BY + AZ*BZ

         VMOD=(A+B)/(A*B*(A*B + ADB))

         VXD=VXD + DUB*VMOD*AVBX

         VYD=VYD + DUB*VMOD*AVBY

         VZD=VZD + DUB*VMOD*AVBZ

C TOTAL

         VX=VXD+VXS

         VY=VYD+VYS

         VZ=VZD+VZS

20       CONTINUE

       TVS=SQRT(VXS*VXS+VYS*VYS+VZS*VZS)

       TPVS=SQRT(PVXS*PVXS+PVYS*PVYS+PVZS*PVZS)

       TVD=SQRT(VXD*VXD+VYD*VYD+VZD*VZD)

       TPVD=SQRT(PVXD*PVXD+PVYD*PVYD+PVZD*PVZD)

       TV=SQRT(VX*VX+VY*VY+VZ*VZ)

       IF(LLL.EQ.4)THEN

         IF(PX.LE.0.0)THEN

           PDI=-SQRT(PX*PX+PY*PY)

         ELSE

           PDI=SQRT(PX*PX+PY*PY)

         ENDIF

       ENDIF

     IF(LLL.LE.2)WRITE(6,*)'RADIUS=',RDIST
```

```
      IF(LLL.EQ.3)WRITE(6,*)'X-AXIS=',PX
      IF(LLL.EQ.4)WRITE(6,*)'XY-PLANE=',PDI
      WRITE(6,*)'CASE=',LLL
      WRITE(6,*)'SOURCE ONLY:'
      WRITE(6,*)'TOTAL=',TVS
      WRITE(6,*)'POINT SOURCE ONLY:'
      WRITE(6,*)'TOTAL=',TPVS
      WRITE(6,*)'DOUBLET ONLY:'
      WRITE(6,*)'TOTAL=',TVD
      WRITE(6,*)'POINT DOUBLET ONLY:'
      WRITE(6,*)'TOTAL=',TPVD
      WRITE(6,*)'VX=',VX
      WRITE(6,*)'VY=',VY
      WRITE(6,*)'VZ=',VZ
      WRITE(6,*)'TOTAL=',TV
      IF(LLL.LE.2)WRITE(2,*) RDIST,TVS,TPVS,TVD,TPVD
      IF(LLL.EQ.3)WRITE(2,*) PX,TVS,TPVS,TVD,TPVD
      IF(LLL.EQ.4)WRITE(2,*) PDI,TVS,TPVS,TVD,TPVD
      WRITE(6,*) ' '
      WRITE(6,*) ' '
100   CONTINUE
      CALL EXIT
      END
```

```
SUBROUTINE CASE(LLL,PI,THETA,THE45,DI,PXI,PYI,PZI)

WRITE(6,*)'INPUT LINE INITIAL RADIUS:'

READ(5,*) DI

IF(LLL.GE.3)THETA=45.*PI/180.

IF(LLL.EQ.1.OR.LLL.EQ.3)THEN

   PXI=DI*COS(THETA)

   PYI=0.0

   PZI=DI*SIN(THETA)

ELSE

   PXI=DI*COS(THETA)*THE45

   PYI=DI*COS(THETA)*THE45

   PZI=DI*SIN(THETA)

ENDIF

RETURN

END
```

REFERENCES

1. Rogers, E. W.: Blockage Effects in a Closed or Open Tunnels. AGARDograph No. 109, October 1966.
2. Herriot, J. G.: Blockage Corrections for Three Dimensional-Flow Closed-Throat Wind Tunnels with Consideration of the Effect of Compressibility. NACA TR-995, 1950.
3. Maskell, E. C.: A Theory of the Blockage Effects on Bluff Bodies and Stalled Wings in a Closed Wind Tunnel. Air Research Committee R&M 3400, 1965.
4. Pope, A.; and Rae, W.: Low Speed Wind Tunnel Testing. Second ed. John Wiley and Sons, Inc., 1984, pp. 344-444.
5. Hackett, J.E.; Sampath, S.; and Phillips, C. G.: Determination of Wind Tunnel Constraint Effects by a Unified Pressure Signature Method. Part 1: Applications to Winged Configurations. NASA CR-166186, 1981.
6. Adair, D.; and Horne, W. C.: Characteristics of a Separating Confluent Boundary Layer and the Downstream Wake. NASA TM-100046, 1987.
7. Ashby, D.; Dudley, M.; and Iguchi, S.: Development and Validation of an Advanced Low-Order Panel Method. NASA TM-101024, 1988.
8. Ashby, D.; and Sandlin, D.: Application of a Low Order Panel Method to Complex Three Dimensional Internal Flow Problems. NASA CR-177424, 1986.
9. Maskew, B.: Program VSAERO, A Computer Program for Calculating the Non-Linear Aerodynamic Characteristics of Arbitrary Configurations. NASA CR-4023, 1987.
10. Katz, J.; and Maskew, B.: Unsteady Low-Speed Aerodynamics Model for Complete Aircraft Configurations. AIAA Paper 86-2180-CP, August 1986.
11. Katz, J.: Integration of Computational Methods in Automotive Wind Tunnel Testing. SAE Paper 89-0601, February 1989.
12. Peters, G.E.: F/A-18 Basic Aerodynamic Data. McDonnell Douglas Report MDC-A8575 Revision A, August 1985, pp. 3.5-3.6.
13. Hess, J. L.;and Smith, A. M.: Calculation of Potential Flow About Arbitrary Bodies. Progress in Aeronautical Sciences, Volume 8. Pergamon Press, 1967, pp. 1-138.

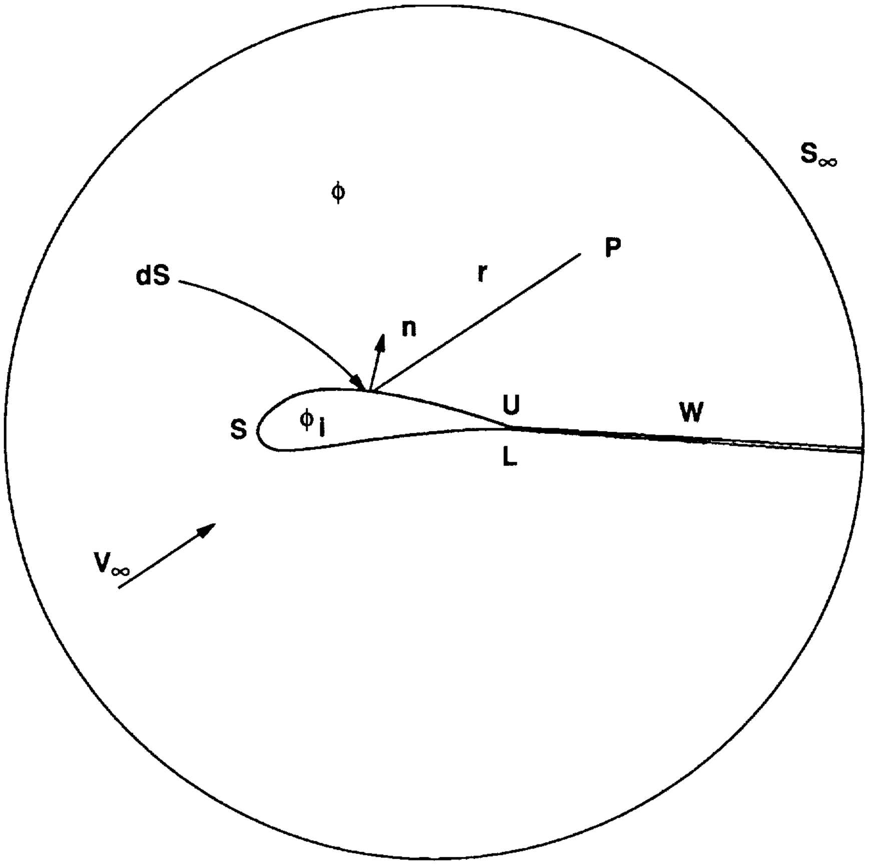

S∞
ϕ
P
r
dS
n
U
W
S
ϕi
L
V∞

Figure 1.– Section through the idealized flow field.

PRECEDING PAGE BLANK NOT FILMED

PAGE 44 INTENTIONALLY BLANK

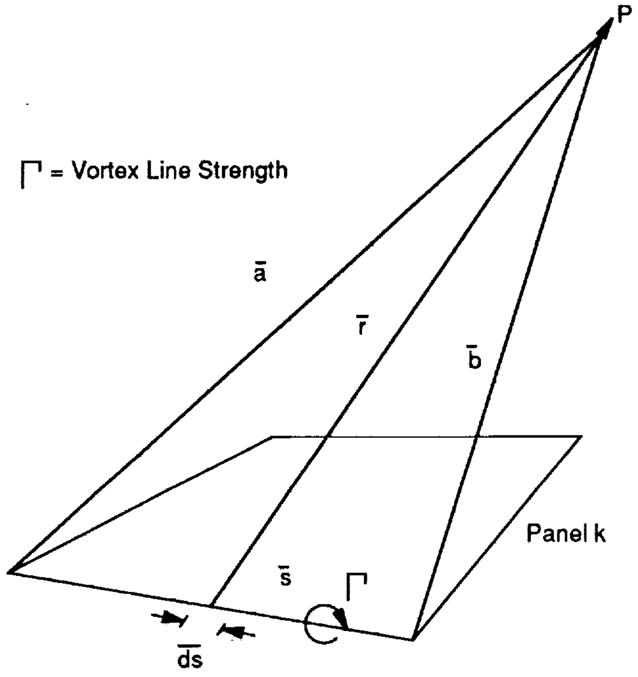
P
Γ = Vortex Line Strength
$\bar{a}$
$\bar{r}$
$\bar{b}$
Panel k
$\bar{s}$
Γ
$\overline{ds}$

Figure 2.– Line vortex geometry.

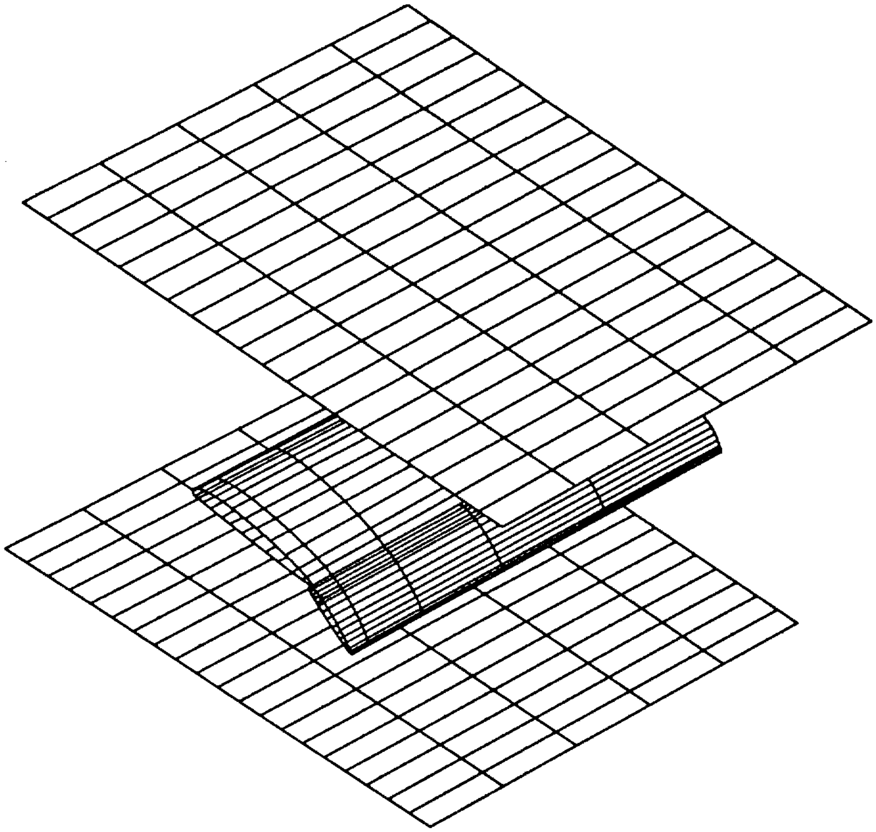

Figure 3.– Section of the two-dimensional PMARC model.

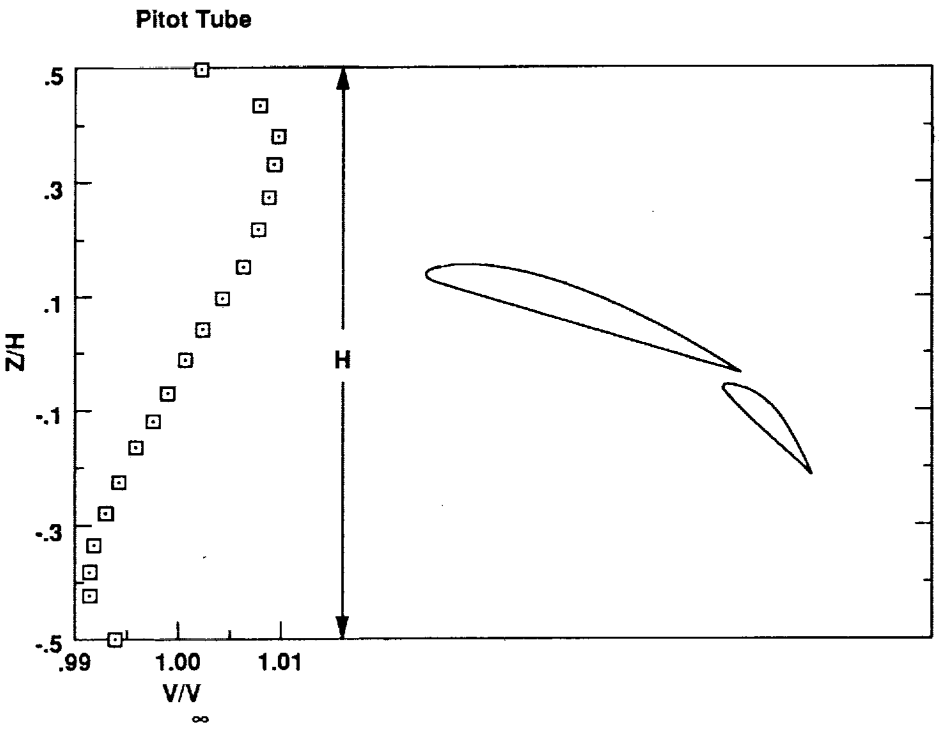

Figure 4.– Computed velocity profile at the test section centerline.

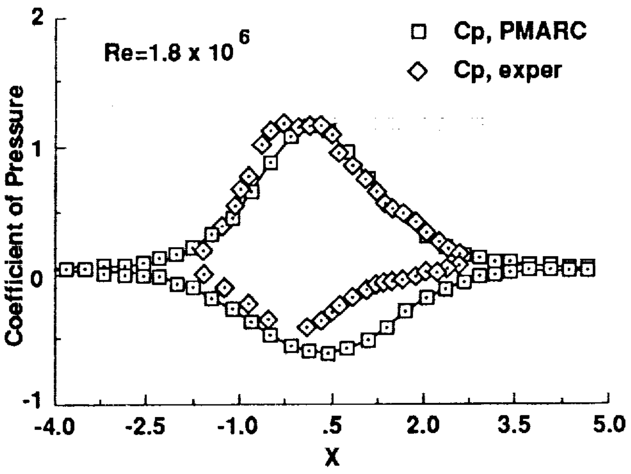

Figure 5.– Pressure distribution, tunnel.

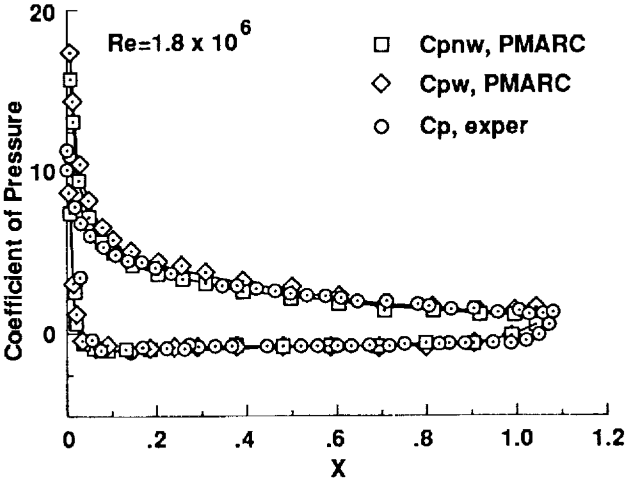

Figure 6.– Pressure distribution, wing.

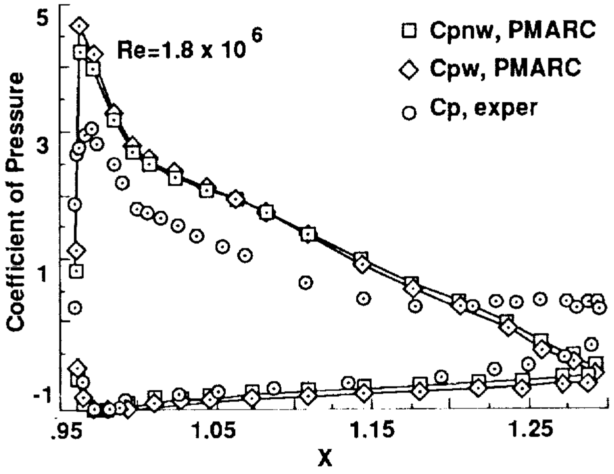

Figure 7.– Pressure distribution, flap.

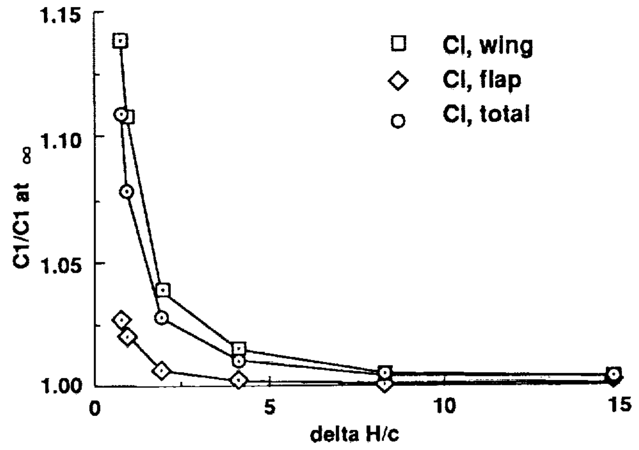

Figure 8.– Lift decrease as a function of tunnel height.

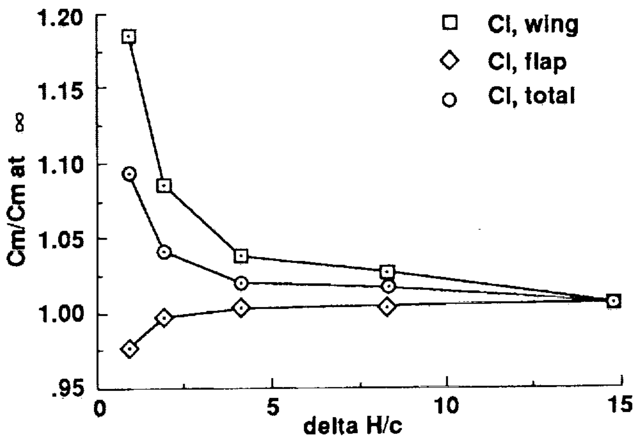

Figure 9.– Pitching moment increase as a function of tunnel height.

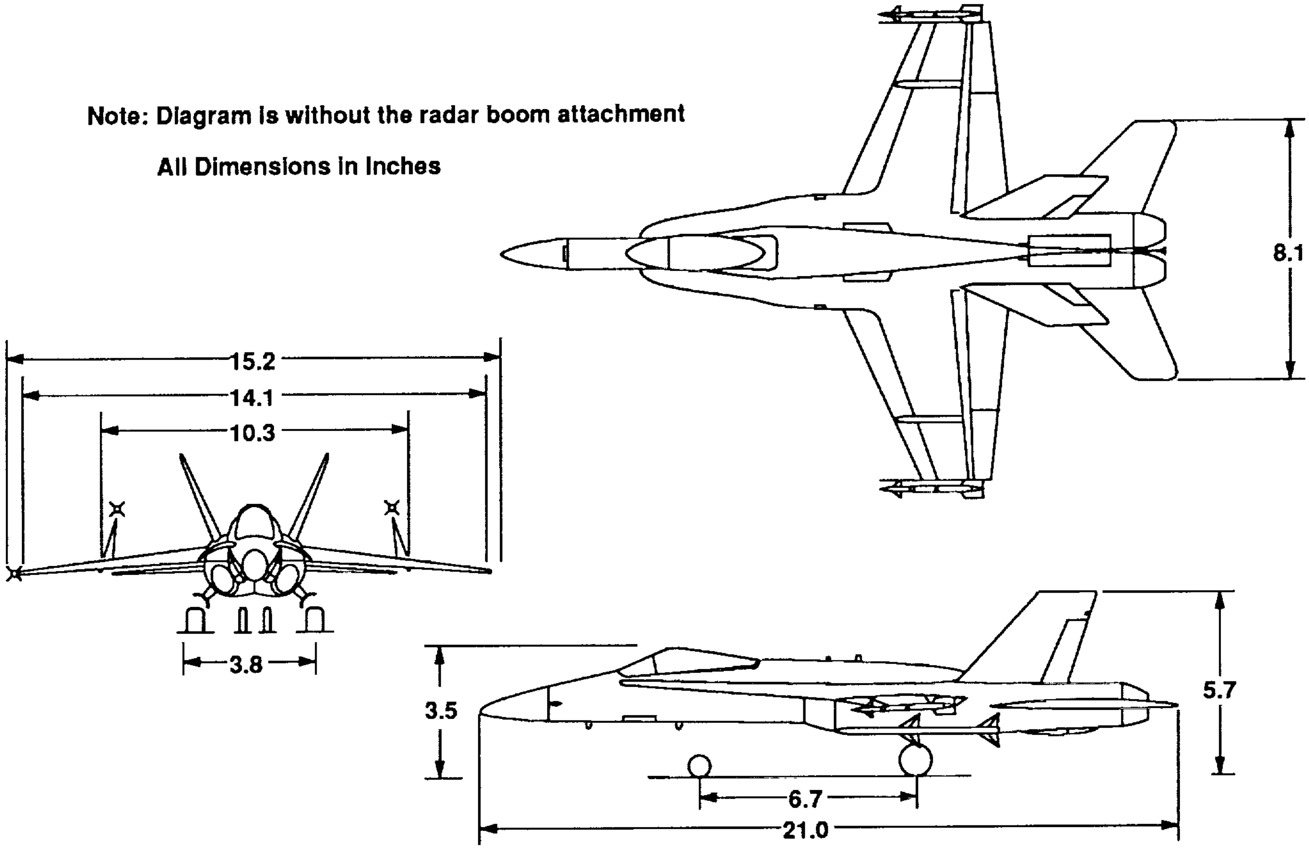
Note: Diagram is without the radar boom attachment
All Dimensions in Inches
15.2
14.1
10.3
3.8
8.1
3.5
5.7
6.7
21.0

Figure 10.– McDonnell Douglas F/A-18 model.

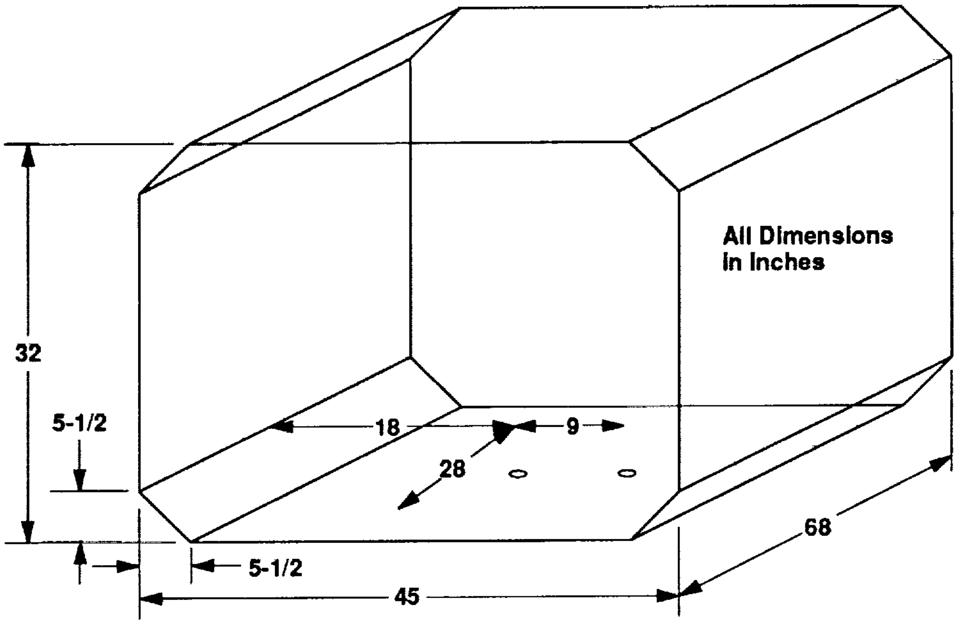
All Dimensions in Inches
32
5-1/2
18
9
28
5-1/2
45
68

Figure 11.– Test section geometry.

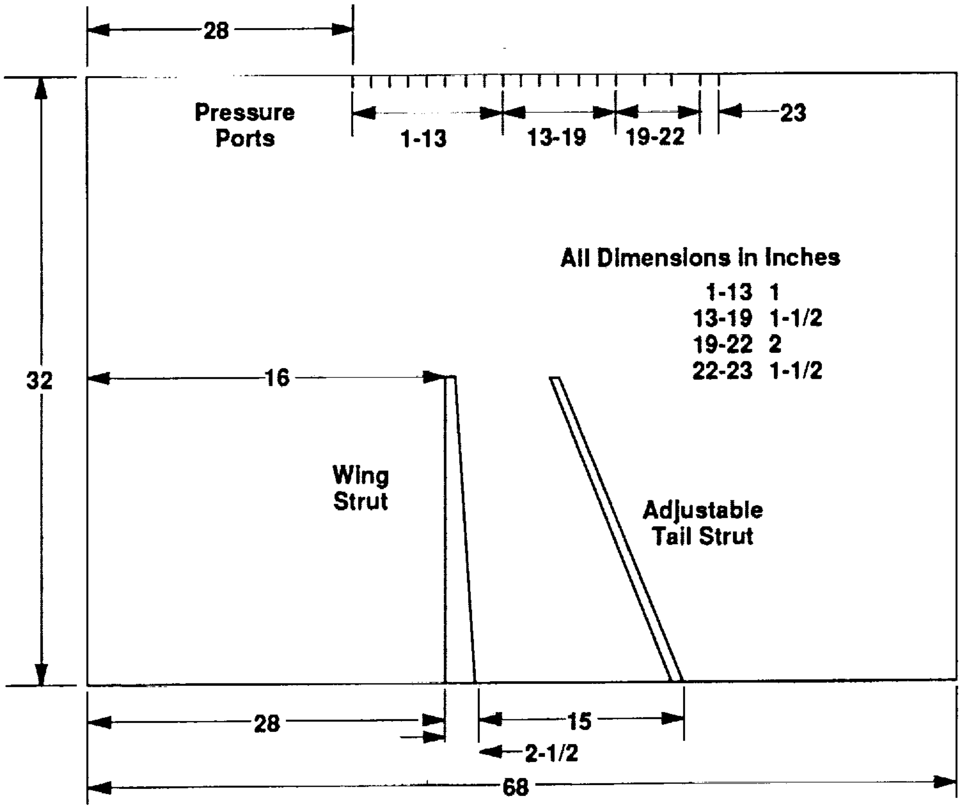
28
Pressure Ports
1-13
13-19
19-22
23
All Dimensions in Inches
1-13 1
13-19 1-1/2
19-22 2
22-23 1-1/2
32
16
Wing Strut
Adjustable Tail Strut
28
15
2-1/2
68

Figure 12.– Wind tunnel cross section.

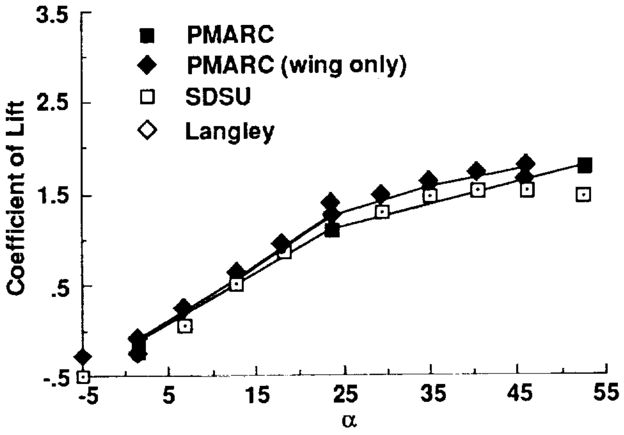

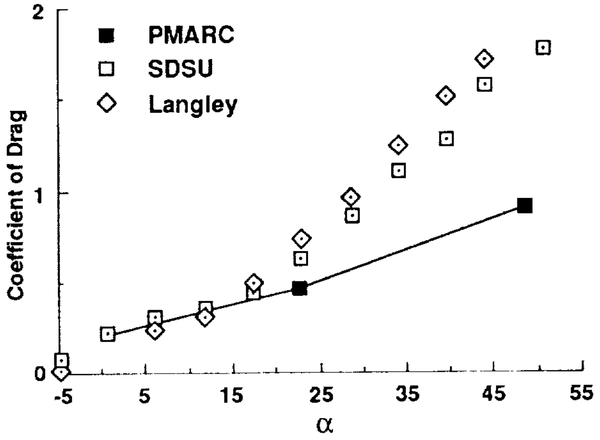

Figure 13.– Aerodynamic characteristics of the F/A-18.

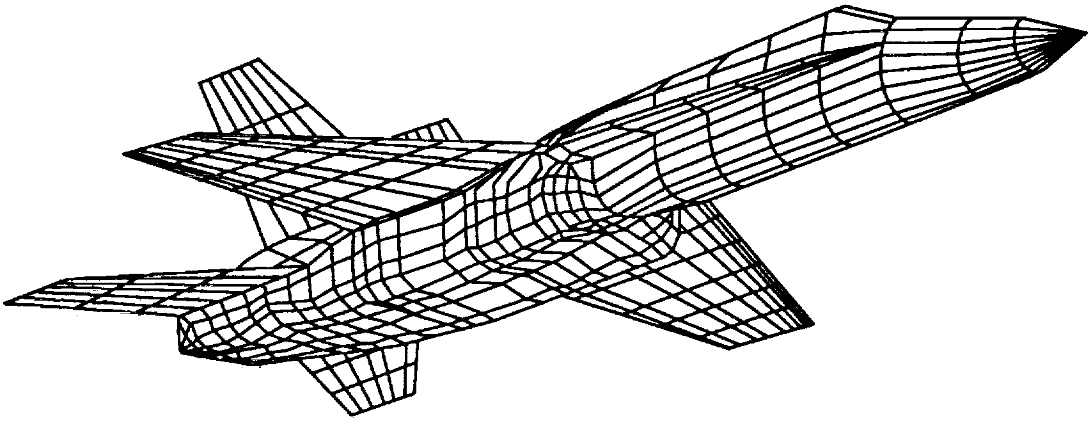

Figure 14.– F/A-18 paneled model from McDonnell Douglas.

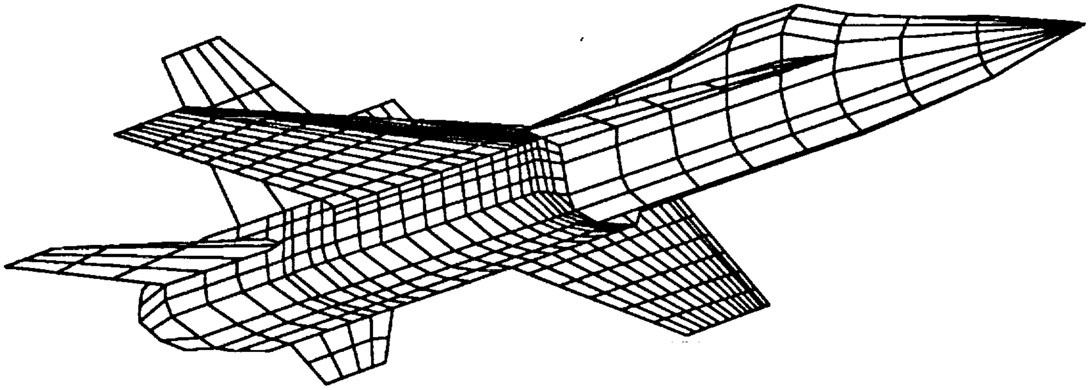

Figure 15.– F/A-18 paneled model after rework.

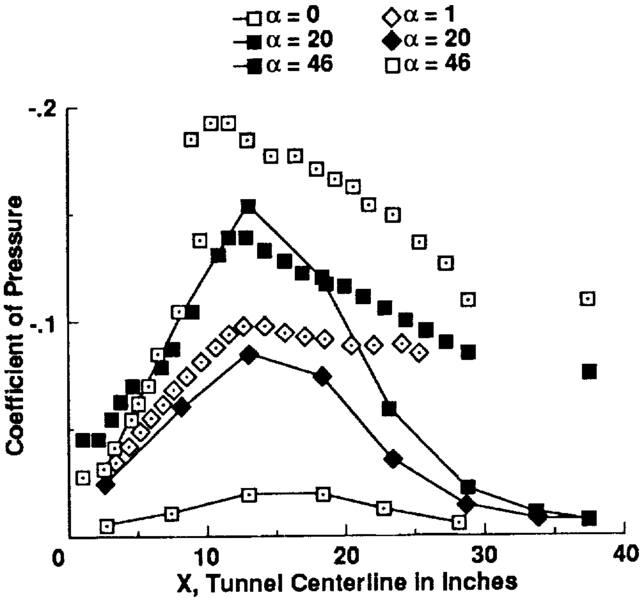

Figure 16.– Pressure distribution, tunnel upper wall.

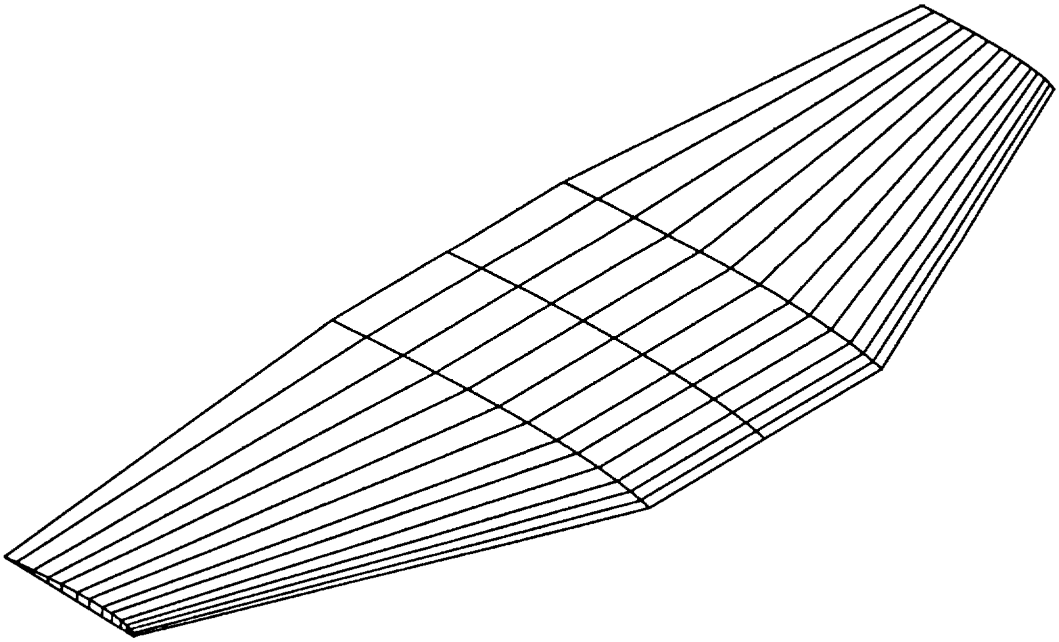

Figure 17.– F/A-18, wing only.

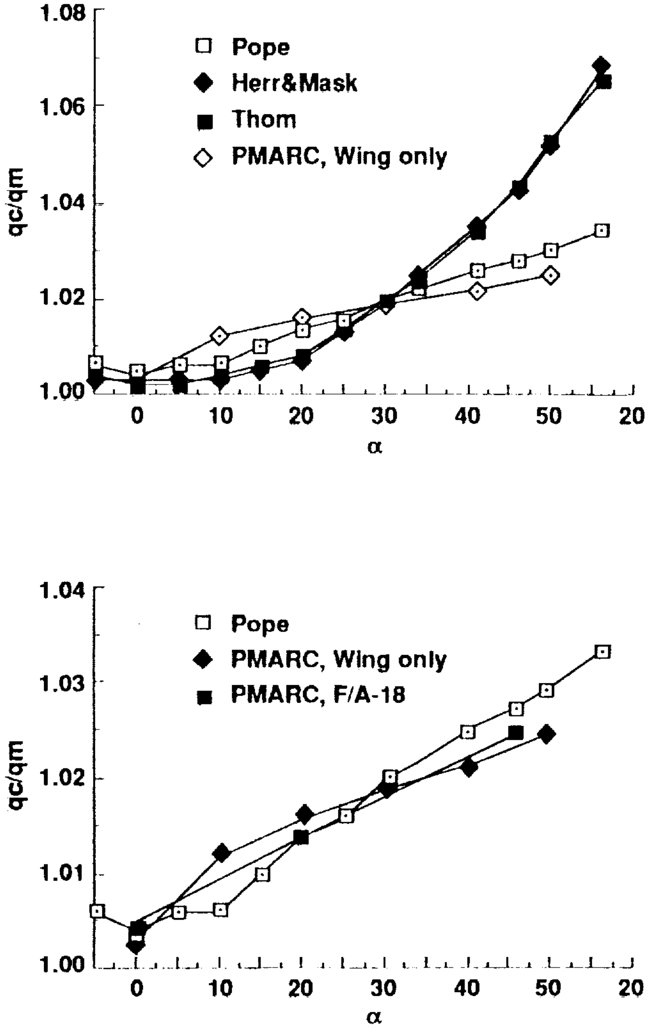

Figure 18.– Wall correction comparison.

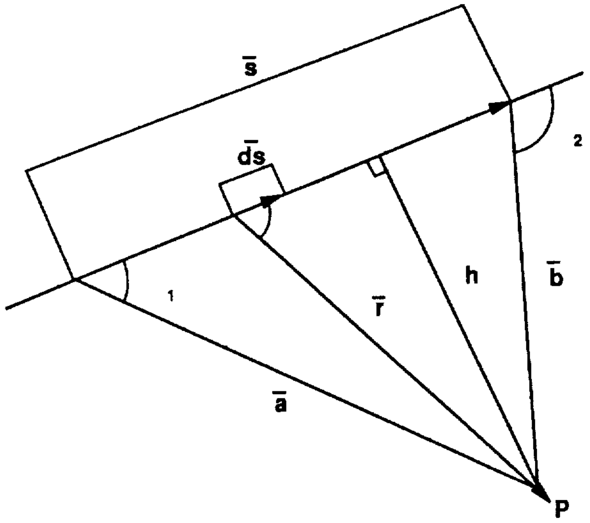

$\bar{s}$
$\bar{ds}$
2
1
h
$\bar{b}$
$\bar{r}$
$\bar{a}$
P

Figure 19.– Vector orientation.

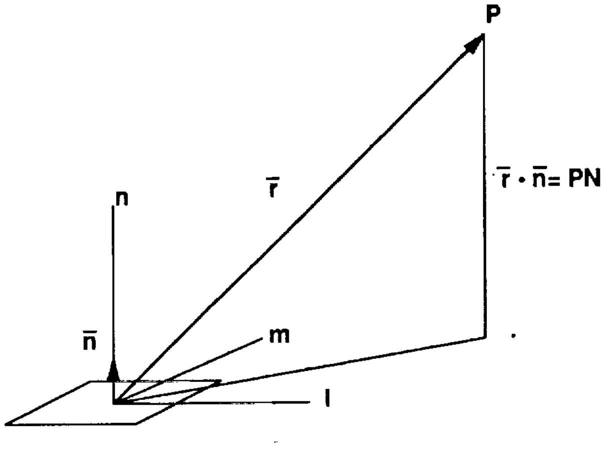

P
$\bar{r} \cdot \bar{n}$= PN
n
$\bar{r}$
$\bar{n}$
m
l

Figure 20.– Panel orientation.

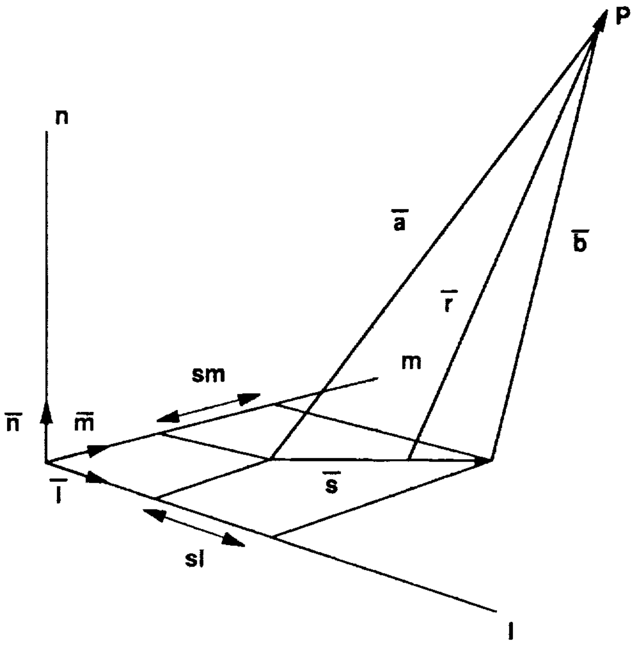
P
n
$\bar{a}$
$\bar{b}$
$\bar{r}$
m
sm
$\bar{n}$
$\bar{m}$
$\bar{l}$
$\bar{s}$
sl
l

Figure 21.– Vector orientation in the panel plane.

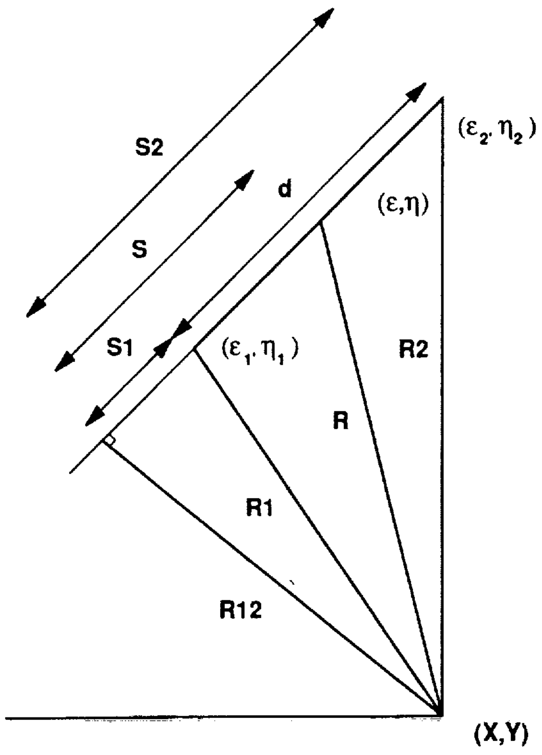
S2
d
S
S1
(ε_2, η_2)
(ε, η)
(ε_1, η_1)
R2
R
R1
R12
(X,Y)

Figure 22.– Source derivation geometry.

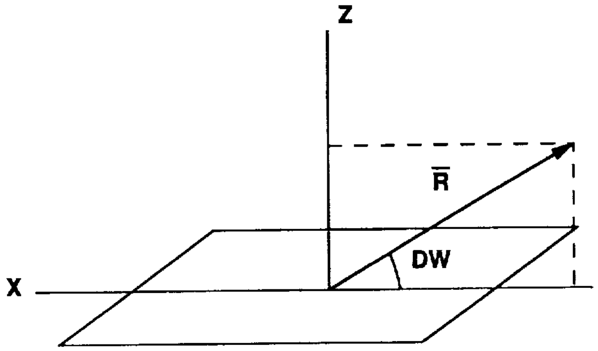

Figure 23.– Point orientation, over median.

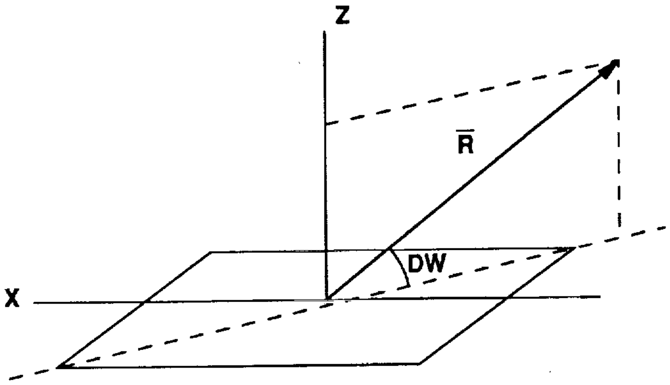

Figure 24.– Point orientation, over horizontal.

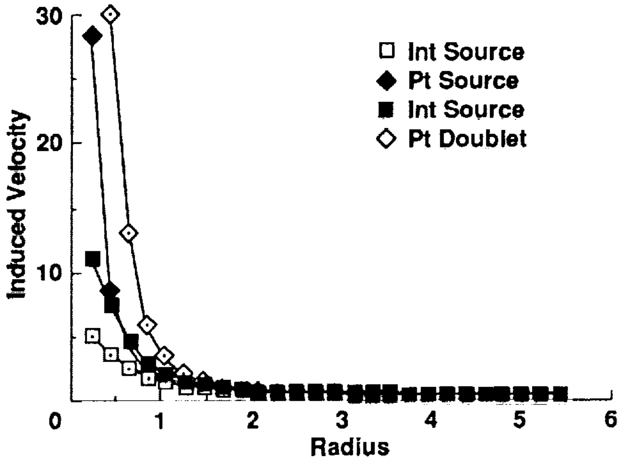

Figure 25.– Over median, DW = 90°.

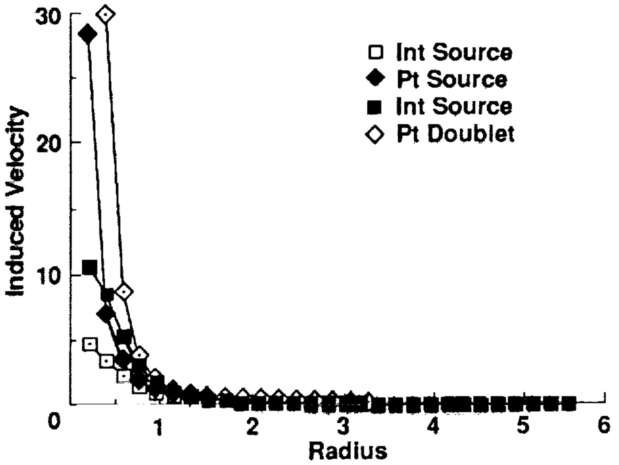

Figure 26.– Over median, DW = 45°.

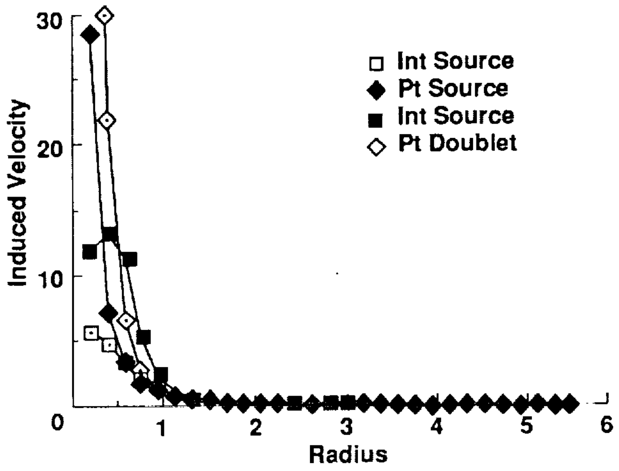

Figure 27.– Over horizontal, DW = 20°.

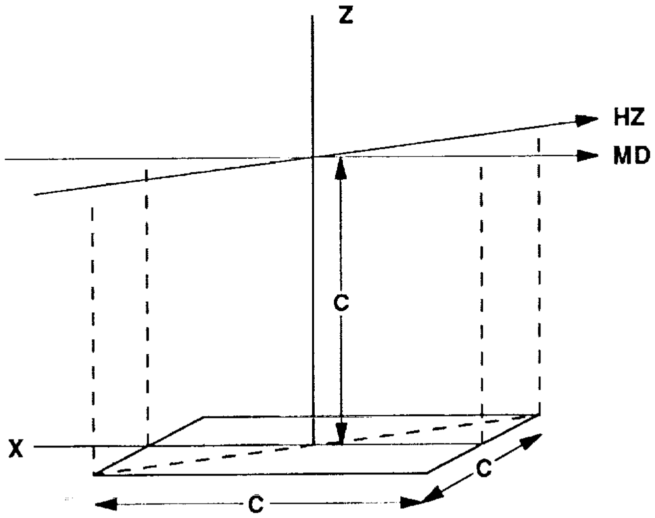

Figure 28.– Panel transverse, over horizontal (HZ) and over median (MD).

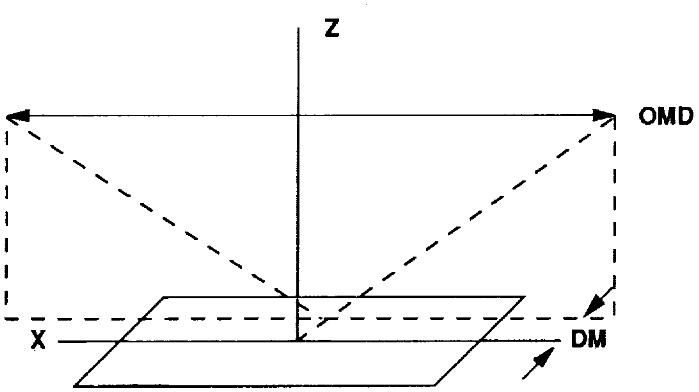

Figure 29.– Panel transverse, over off-median.

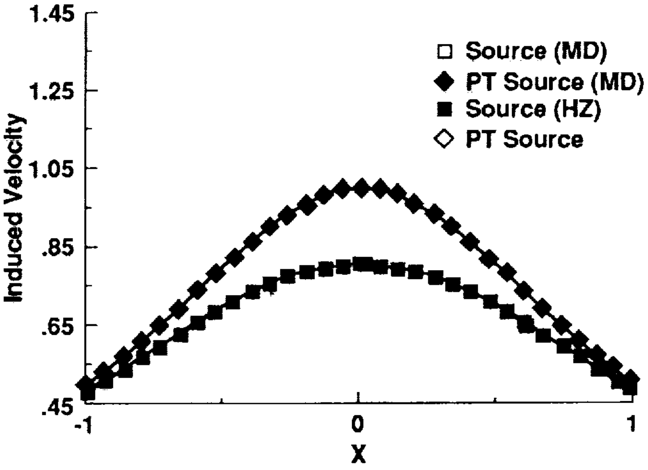

Figure 30.– Panel transverse, source contribution.

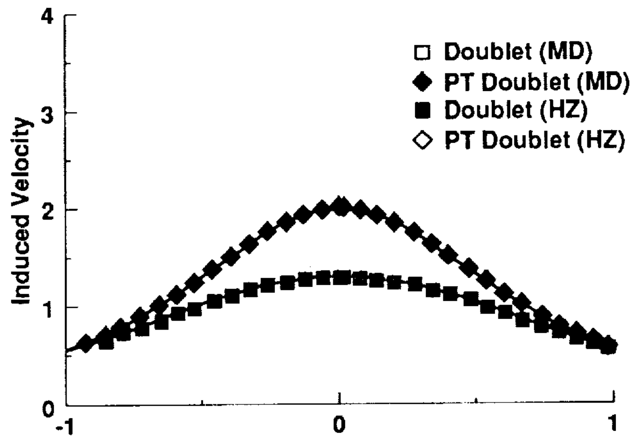

Figure 31.– Panel transverse, doublet contribution.

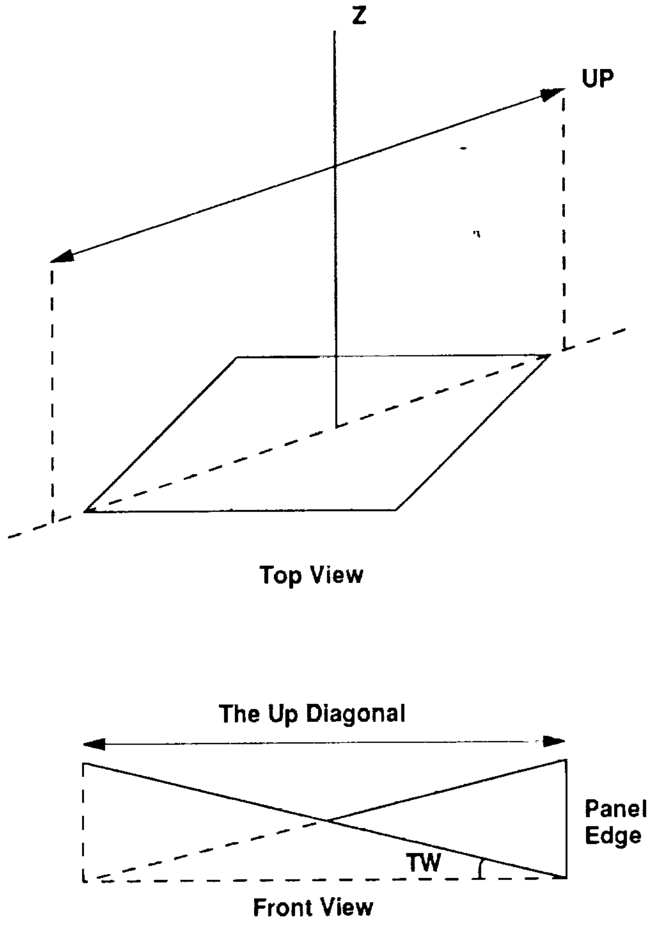

Z
UP
Top View
The Up Diagonal
Panel Edge
TW
Front View

Figure 32.– Twisted panel orientation, UP = over the Up diagonal.

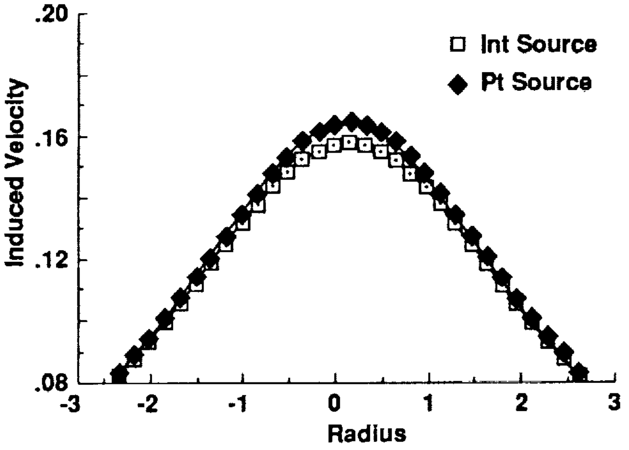

Figure 33.– Twisted panel, TW = 0°.

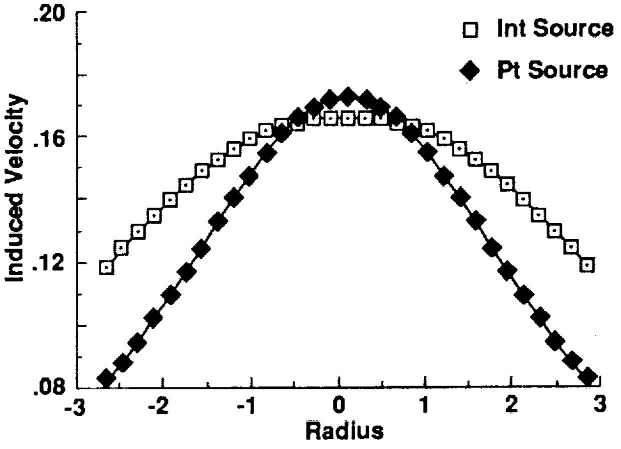

Figure 34.– Twisted panel, TW = 10°.

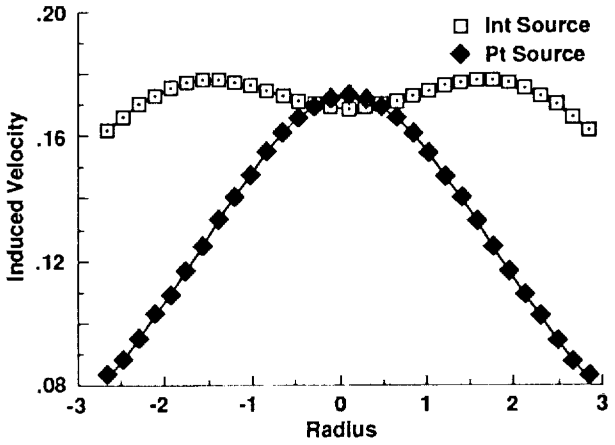

Figure 35.– Twisted panel, TW = 20°.

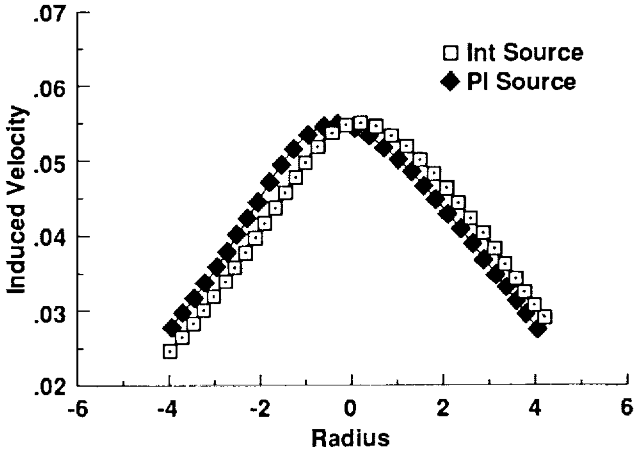

Figure 36.– Off median, DM = 0.25, TW = 10°.

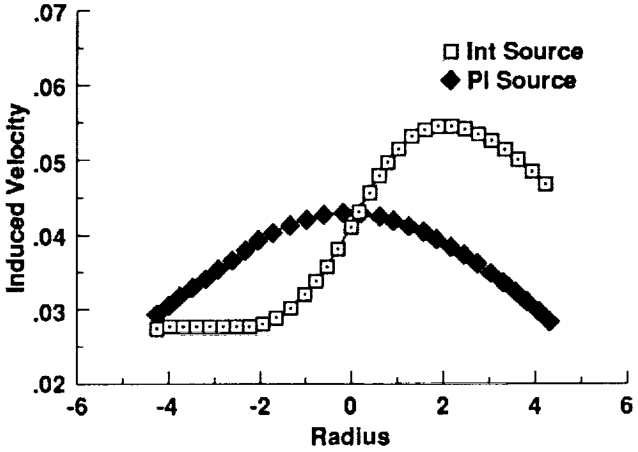

Figure 37.– Off median, DM = 3, TW = 10°.

NASA
National Aeronautics and Space Administration

Report Documentation Page

1. Report No. NASA TM-102196	2. Government Accession No.	3. Recipient's Catalog No.
4. Title and Subtitle Study of the Integration of Wind Tunnel and Computational Methods for Aerodynamic Configurations		5. Report Date October 1989
		6. Performing Organization Code
7. Author(s) Lindsey E. Browne and Dale L. Ashby		8. Performing Organization Report No. A-89148
		10. Work Unit No. 505-68-71
9. Performing Organization Name and Address Ames Research Center Moffett Field, CA 94035		11. Contract or Grant No.
		13. Type of Report and Period Covered Technical Memorandum
12. Sponsoring Agency Name and Address National Aeronautics and Space Administration Washington, DC 20546-0001		14. Sponsoring Agency Code

15. Supplementary Notes

Point of Contact: Dale L. Ashby, Ames Research Center, MS 247-2, Moffett Field, CA 94035
(415) 694-5047 or FTS 464-5047

16. Abstract

A study was conducted to determine the effectiveness of using a low-order panel code to estimate wind tunnel wall corrections. The corrections were found by two computations. The first computation included the test model and the surrounding wind tunnel walls, while in the second computation the wind tunnel walls were removed. The difference between the force and moment coefficients obtained by comparing these two cases allowed the determination of the wall corrections. The technique was verified by matching the test-section, wall-pressure signature from a wind tunnel test with the signature predicted by the panel code. To prove the viability of the technique, two cases were considered. The first was a two-dimensional high-lift wing with flap that was tested in the 7- by 10-Foot Wind Tunnel at NASA Ames Research Center. The second was a 1/32-scale model of the F/A-18 aircraft which was tested in the low-speed wind tunnel at San Diego State University. The panel code used was PMARC (Panel Method Ames Research Center). Results of this study indicate that the proposed wind tunnel wall correction method is comparable to other methods and that it also inherently includes the corrections due to model blockage and wing lift.

17. Key Words (Suggested by Author(s)) Wind tunnel Computational Aerodynamic	18. Distribution Statement Unclassified-Unlimited Subject Category - 02

19. Security Classif. (of this report) Unclassified	20. Security Classif. (of this page) Unclassified	21. No. of Pages 71	22. Price A04

NASA FORM 1626 OCT 86

For sale by the National Technical Information Service, Springfield, Virginia 22161